JOURNAL OF GEOPHYSICAL RESEARCH, VOL. 111, D14S92, doi:10.1029/2005JD006720, 2006

Click Here for Full Article

Mesoscale modeling of Central American smoke transport to the United States: 2. Smoke radiative impact on regional surface energy budget and boundary layer evolution

Jun Wang[1,2] and Sundar A. Christopher[1]

Received 28 September 2005; revised 16 December 2005; accepted 3 March 2006; published 26 July 2006.

[1] During 20 April to 21 May 2003, large amounts of smoke aerosols from Central American Biomass Burning (CABB) fires were transported to southeastern United States. Using a coupled aerosol, radiation, and meteorology model built upon the heritage of the Regional Atmospheric Modeling System (RAMS) with new capabilities called the Assimilation and Radiation Online Modeling of Aerosols (AROMA), this paper, the second of a two-part series, investigates smoke radiative impact on the regional surface energy budget, temperature and relevant boundary layer processes. Comparisons with limited ground-based observations and MODIS aerosol optical thickness (AOT) showed that model consistently simulated the smoke AOT and smoke radiative impacts on the 2 m air temperature (2mT) and downward shortwave irradiance (DSWI). Over 30 days the 24-hour mean smoke AOT was 0.18 (at 0.55 μm) near the smoke source region (Yucatan Peninsula and southern Mexico), and 0.09 in downwind region (e.g., southern Texas), both showing a diurnal variation of 24%. Maximum AOT occurred during late afternoon and minimum during early morning in smoke source region. The smoke radiative effects were dominant mostly during the daytime and resulted in the decrease of DSWI, sensible heat and latent heat by 22.5 Wm^{-2}, 6.2 Wm^{-2}, and 6.2 Wm^{-2}, respectively, near the source region, in contrast to 15.8 Wm^{-2}, 4.7 Wm^{-2}, and 7.9 Wm^{-2}, respectively, in downwind regions. Both maximum and minimum 2mT were decreased, and the overall diurnal temperature range (DTR) was reduced by 0.31°C and 0.26°C in the smoke source and downwind regions, respectively. The smoke absorption of solar radiation increased the lapse rate by 0.1–0.5 K/day in the planetary boundary layer (PBL), thus warming the air over the ocean surface. However, over the land surface where the coupling between the lower PBL and the cooler land surface is strong, such warming only occurred in the upper PBL and is amendable to the diurnal variation of smoke emission. The simulation numerically verifies the smoke self-trapping feedback mechanism proposed by Robock (1988), where the increase of the atmospheric stability in the PBL caused by the smoke radiative effects further traps more smoke aerosols in the lower PBL. Such feedbacks, when coupled with favorable synoptic systems, may have important implications for air quality modeling and hydrological processes.

Citation: Wang, J., and S. A. Christopher (2006), Mesoscale modeling of Central American smoke transport to the United States: 2. Smoke radiative impact on regional surface energy budget and boundary layer evolution, *J. Geophys. Res.*, *111*, D14S92, doi:10.1029/2005JD006720.

1. Introduction

[2] Widely occurring in the tropics, biomass burning is one of the largest sources of anthropogenic aerosols [*Crutzen and Andreae*, 1990]. Burning mostly occurs during the tropical dry season (e.g., April–June in the northern hemisphere and August–October in the southern hemisphere), and ends when wet season begins [*Crutzen et al.*, 1979]. Smoke particles from burning fires degrade the visibility and air quality in both source and downwind regions [*Peppler et al.*, 2000], and have important implications for climate and weather forecasting, since they affect the atmospheric radiative transfer both directly (by scattering the sunlight) and indirectly (by acting as cloud condensation nuclei) [*Twomey*, 1977; *Penner et al.*, 1992]. In addition, the black carbon in smoke particles strongly

[1]Department of Atmospheric Science, University of Alabama, Huntsville, Alabama, USA.
[2]Now at Division of Engineering and Applied Science and Department of Earth and Planetary Science, Harvard University, Cambridge, Massachusetts, USA.

Copyright 2006 by the American Geophysical Union.
0148-0227/06/2005JD006720$09.00

absorb solar radiation [*Jacobson*, 2001], thereby enhancing the atmospheric radiative heating rate, modifying the atmospheric stability [*Robock*, 1988] and altering cloud formation [*Ackerman et al.*, 2000; *Koren et al.*, 2004], which can possibly result in measurable changes in precipitation distribution [*Menon et al.*, 2002]. Accurate representation of smoke radiative impacts is crucial for the prediction of climate and weather [*Ramanathan et al.*, 2001; *Intergovernmental Panel on Climate Change* (*IPCC*), 2001], particularly during the biomass-burning season in regional scales [*Westphal and Toon*, 1991; *Kaufman et al.*, 1998; *Swap et al.*, 2003].

[3] During April–May 2003, under the influence of southerly flow, large amounts of smoke aerosols from the Central American Biomass Burning (CABB) were transported across the Gulf of Mexico and reached the Texas, Oklahoma, and other nearby areas in the southeastern United States (SEUS) [*Wang et al.*, 2006]. The events are the second largest in the last decade in this region (after the May 1998 CABB events [*Peppler et al.*, 2000]), and resulted in the largest $PM_{2.5}$ (particulate matter with aerodynamic diameter less than 2.5 μm) mass concentration measured in southern Texas since 1998 [*Wang et al.*, 2006]. The intent of this study is to investigate the direct radiative impacts of smoke events on the surface energy budget, air temperature, and evolution of planetary boundary layer (PBL) in both the source and downwind regions.

[4] A wealth of previous studies using combinations of measurements and chemistry transport models (CTM), have been carried out to examine smoke radiative impacts, particularly in quantifying the direct smoke radiative forcing at the top of atmosphere (TOA) (see *IPCC* [2001, section 6.7.5] for a review). These studies reported that the TOA global direct radiative forcing of biomass-burning smoke aerosols is -0.2 Wm^{-2} with an uncertainty of at least of 300%. However, the magnitude could be one to two orders larger in the smoke source region during biomass-burning seasons. While smoke radiative forcing at TOA is important, equally important is the forcing at the surface as well as in the atmosphere. Both model calculations and measurements have showed that the smoke radiative forcing at the surface is about 2∼3 times larger than the forcing at TOA due to the enhancement by smoke absorption in the atmosphere [*Christopher et al.*, 2000; *Schafer et al.*, 2002]. The importance of such forcing on the surface energy budget and PBL evolution has been noted by numerous earlier studies [e.g., *Atwater et al.*, 1971a, 1971b; *Bergstrom*, 1973; *Ackerman*, 1977; *Carlson and Benjamin*, 1980]. Recently, *Yu et al.* [2002] showed that, for a smoke layer with aerosol optical thickness (AOT) of 0.5 and single scattering albedo larger than 0.9 in the PBL, absorption of solar radiation can increase the daytime radiative heating in the PBL up to 52 Wm^{-2}, and its extinction on the downward shortwave irradiance (DSWI) can result in the decrease of surface skin temperature more than 1 K. They further showed that these changes, when coupled with the PBL processes, can cause measurable decrease of PBL height (PBLH) and diurnal temperature range (DTR). While these studies advanced our understanding on the aerosol radiative impacts in the lower troposphere, they were carried out in a "1D" column framework (e.g., no horizontal advection). In contrast, CTMs reasonably simulate the 3D aerosol distribution at regional and global scales [*Liousse et al.*, 1996; *Tegen et al.*, 1997; *Chin et al.*, 2002; *Park et al.*, 2003; *Carmichael et al.*, 2003; *Colarco et al.*, 2004], but most of them are driven by meteorological fields (such as winds) from offline meteorological models. As such, coupling the aerosol transport and aerosol radiation with a 3D meteorological model would be important for further investigation on the meteorological responses to the smoke radiative effects [*Westphal and Toon*, 1991; *Wang et al.*, 2004].

[5] In traditional meteorological models, aerosol radiative impacts are not explicitly treated, because aerosol distribution with high spatiotemporal variations is not readily available in the model [*Stephens*, 1984]. This could cause large uncertainties in the simulation of surface energy budget, particularly during the smoke or dust episodes [*Ackerman and Cox*, 1982; *Stephens*, 1984; *Cautenet et al.*, 1992; *Chen et al.*, 1995]. *Robock* [1988] reported that smoke emitted from forest fires in northern California in September 1987 was trapped in a valley by an inversion layer for nearly 3 weeks. This smoke layer decreased the daily maximum air temperature near the surface by more than 15°C below normal conditions for about 1 week and more than 5°C for 3 weeks. He proposed that the maintenance of this long-term inversion layer was due a positive feedback loop where the smoke layer blocks the solar radiation from reaching the surface while absorbing the solar energy in the atmosphere, thus triggering a favorable mechanism for the temperature inversion that in turn enhances the smoke trapping. *Westphal and Toon* [1991] showed a case study where the surface temperature was decreased by 5°C during the passage of smoke plumes from a boreal fire in 1988. In the Nashville southern oxidants studies in 1995 and 1999, *Zamora et al.* [2003] found that the incorrect (neglecting) specification of aerosol scattering and absorption in the Fifth-Generation Penn State/NCAR Mesoscale Model (MM5) can lead to an overestimation of DSWI by 100 Wm^{-2}, and suggested that aerosol radiative process is important for both meteorological and air quality forecasting. Recently, *Grell et al.* [2004] has proposed to incorporate the aerosol-radiation interaction in the Weather Research and Forecast (WRF) model, and *Wang et al.* [2004] have reported improvement in the simulation of surface energy budget and air temperature during the dust transport after incorporating the dust radiative impacts in the Regional Atmospheric Modeling System (RAMS).

[6] Since aerosol radiative effects are absent in most standard mesoscale meteorological models such as MM5 [*Grell et al.*, 1995] or RAMS [*Harrington and Olsson*, 2001; *Cotton et al.*, 2003], previous studies have employed climate models (such as Community Climate Model CCM3) to investigate the smoke radiative impacts [*Chung and Zhang*, 2004; *Davison et al.*, 2004]. However, these investigations usually lack detailed treatment of smoke temporal variations, i.e., smoke distribution and vertical profile were either specified as time-invariant [*Chung and Zhang*, 2004] or were simulated by adopting the constant smoke emission rate [*Davison et al.*,2004]. Such simplification may lead to considerable uncertainties in the model results, because aerosol radiative impact highly depends on the solar zenith angle [*Christopher and Zhang*, 2002] as well as the aerosol vertical distribution [*Yu et al.*, 2002; *Feingold et al.*, 2005], both amenable to the distinct diurnal behavior of biomass-

burning activities with peak in the noon time and minimum during the night [*Prins et al.*, 1998]. Using data collected in southern Africa during the Southern African Regional Science Initiative (SAFARI) campaign, *Eck et al.* [2003] reported that such fire behavior can lead to a 25% systemic diurnal variation of smoke AOT with maximum (minimum) at local 1800 LT (1000 LT) near the smoke source region even over a monthly scale.

[7] In this study, we investigate the CABB smoke radiative impacts and feedbacks using a coupled aerosol-radiation-meteorology model, a modified version of RAMS with newly developed capabilities of Assimilation and Radiation Online Modeling of Aerosols (RAMS-AROMA) [*Wang et al.*, 2004, 2006]. RAMS-AROMA couples the aerosol radiation and aerosol transport together with meteorology [*Wang et al.*, 2004], and realistically specifies the diurnal variation of the smoke emission rate by assimilating the hourly geostationary satellite-derived smoke emission product into the model [*Wang et al.*, 2006]. In the first of this two-part series study [*Wang et al.*, 2006], we have used RAMS-AROMA to simulate the CABB smoke transport during 20 April to 21 May 2003, and showed that the simulation was able to capture diurnal variation of AOT in the smoke source region. Comparison with a variety of ground measurements such as $PM_{2.5}$ concentration, carbon mass concentration and AOT, demonstrated the success of RAMS-AROMA in simulating the spatiotemporal variations of smoke distribution [*Wang et al.*, 2006].

[8] Since a comprehensive validation of RAMS-AROMA performance in modeling the smoke distribution has been conducted by *Wang et al.* [2006], in this paper we will study the smoke radiative impacts mainly on the basis of the analysis of model results. Similar to previous studies [*Westphal and Toon*, 1991; *Menon et al.*, 2002; *Davison et al.*, 2004; *Chung and Zhang*, 2004], this study uses RAMS-AROMA to examine the large-scale aerosol radiative impacts on surface energy budget and feedbacks on atmospheric processes that otherwise would be difficult to investigate from observations alone. A brief description of the model, experiment design and data used for the validation is given in section 2. Results are presented in section 3 and the discussion and conclusion are given in section 4.

2. Model Description, Experiment Design, and Data Used

2.1. Model Description

[9] The RAMS-AROMA is developed upon the RAMS 4.3 [*Pielke et al.*, 1992], and a detailed description is given by *Wang et al.* [2004, 2006] and *Wang* [2005]. In RAMS-AROMA, a δ-4 Stream (4S) Radiative Transfer Model (RTM) [*Fu and Liou*, 1993] is embedded in place of the original two-stream RTM to take into account the impact of both cloud and aerosol on the radiative transfer. While the RAMS4.3 has a tracer advection module that can be used to simulate the aerosol transport, it does not include any aerosol deposition or source functions. In RAMS-AROMA, we have added several components for modeling aerosol wet and dry deposition processes. More importantly we have developed the assimilation routine of using GOES-derived hourly smoke emission data [*Reid et al.*, 2004; *Prins et al.*, 1998] for specifying the smoke source function [*Wang et al.*, 2006]. In summary, RAMS-AROMA not only maintains all the functionalities of RAMS4.3 (e.g., meteorological forecast), but also has new capabilities to simulate the aerosol fields and accounts for the aerosol radiative impacts explicitly at each time step and in each model grid. With this design, the aerosol radiative impacts are directly tied to the simulated physical processes in the atmosphere, allowing the dynamical processes in the model to impact aerosol transport and vice versa.

[10] In calculating the smoke radiative impacts, wavelength-dependent smoke optical properties (such as single scattering albedo, extinction cross section and asymmetric factor) are needed to convert the smoke mass concentration into the smoke AOT, and are further used in the δ-4S RTM to compute smoke radiative effects. In RAMS-AROMA, the smoke AOT is calculated by

$$\tau = \sum_{i=1}^{K} (Q_m \times C_i \times f(rh_i)) \times \Delta z_i,$$

where i is the index for vertical layers, K is the total number of layers in the model, C is the mass concentration of smoke (gm^{-3}), Q_m is the mass extinction efficiency (m^2g^{-1}) of smoke particles, Δz_i is the thickness (m) of different layers, and $f(rh)$ is the hygroscopic factor as a function of relative humidity (rh) [*Kotchenruther and Hobbs*, 1998]. In this study, we used the smoke optical model developed by *Christopher and Zhang* [2002] where Q_m is calculated on the basis of Mie theory by modeling smoke particles as a black carbon core surrounded by an organic shell. The organic shell is assumed as nonabsorbing with real part index of refraction of 1.5 [*Reid et al.*, 2005]. The refractive index of black carbon is adapted from *Chang and Charalampopoulos* [1990]. The density of black carbon and organic carbon is assumed to be $1.8gcm^{-3}$ and $1.2gcm^{-3}$, respectively. The radius ratio of the core and shell is assumed to be 0.3 with an equivalent mass fraction of black carbon of 4%. To obtain the bulk optical properties, smoke size distribution is assumed to be lognormal with volume mean diameter of 0.3 μm and standard deviation of 1.8 μm. With these parameters, the modeled single scattering albedo at 0.55 μm and 0.67 μm are 0.91 and 0.90 respectively, consistent with values that are mostly used in the current literature (see review paper by *Reid et al.* [2005]). Figure 1 shows the calculated single scattering albedo, asymmetric factor, and mass extinction coefficient at different wavelengths. At 0.55 μm, the mass extinction efficiency is about 4.5 m^2g^{-1}.

2.2. Experiment Design and Data Used

[11] The model configuration is the same as *Wang et al.* [2006] where the simulation started at 1200 UTC on 20 April 2003, and ended at 1200 UTC on 21 May 2003. The vertical intervals are 50 m at the lowest layer and gradually expand upward to the maximum value of 700 m with a stretch ratio of 1.2. With this configuration, our model vertical resolution in the PBL is only slightly coarser than those used in previous large-eddy simulations that are believed to be an ideal tool for simulating the PBL process in detail (e.g., *Feingold et al.* [2005] used 50 m interval for all vertical layers). However, because of our large study

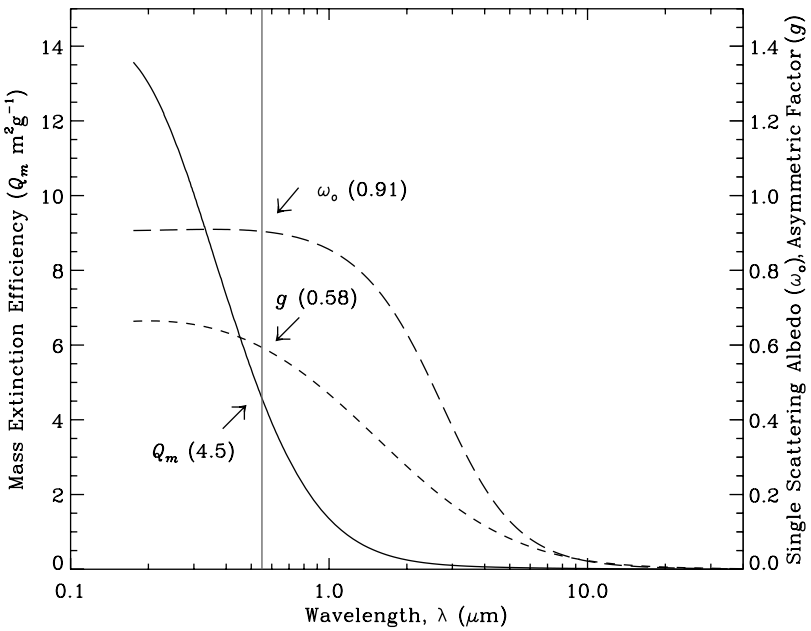

Figure 1. Wavelength-dependent smoke mass extinction efficiency (Q_m, m^2g^{-1}), single scattering albedo (ω_0) and asymmetric factor (g). The numbers in brackets are values at 0.55 μm.

domain (>10^7 km^2, Figure 1), it is beyond the scope of this study to conduct a large eddy simulation that requires a fine horizontal grid resolution on the order of several hundred meters (e.g., 100 m by *Feingold et al.* [2005]). As such, similar to *Wang et al.* [2006], we use two nested grids with horizontal resolution of 120 km and 30 km respectively in the model (Figure 2). Of particular interest in this study are the smoke radiative impacts in the smoke source region (e.g., Yucatan Peninsula) and downwind region (e.g., southern Texas). The model grids that correspond to these two regions are shown in Figure 2.

[12] We select Kuo's cumulus cloud parameterization to represent the subgrid scale cumulus convection [*Walko et al.*, 1995], and Land Ecosystem Atmosphere Feedback (LEAF) module [*Walko et al.*, 2000] to simulate the surface energy budget and air-surface interaction. The level 2.5 turbulent closure model [*Mellor and Yamada*, 1974] is used to simulate the boundary diffusion process. Although this turbulent closure scheme, when applied on a mesh with 30 km horizontal resolution, may be not as good as large eddy simulation studies [e.g., *Feingold et al.*, 2005] in describing the fine structure of turbulence in PBL, it is still physically sound and has been used widely in several mesoscale models (such as in RAMS and MM5). Indeed, *Wang et al.* [2006] found that the RAMS-AROMA, with the above specified configuration, has the capability to capture the general feathers of PBLH evolution (such as the diurnal variation of PBLH and nocturnal boundary layer identified from the time series of lidar-detected aerosol backscattering profile at the ARM site). Such capability is sufficient for the purpose of this study, i.e., to investigate if the smoke radiative impacts on the surface energy budget and PBL processes are statistically important on a large scale. Given the fact that the smoke radiative effects were totally neglected in many current mesoscale models that are usually run in spatial resolution of 20 kms−30 kms, we think that the investigation based on our current model configuration has important ramification for understanding how smoke radiative impacts affect the accuracy of current regional weather or climate models.

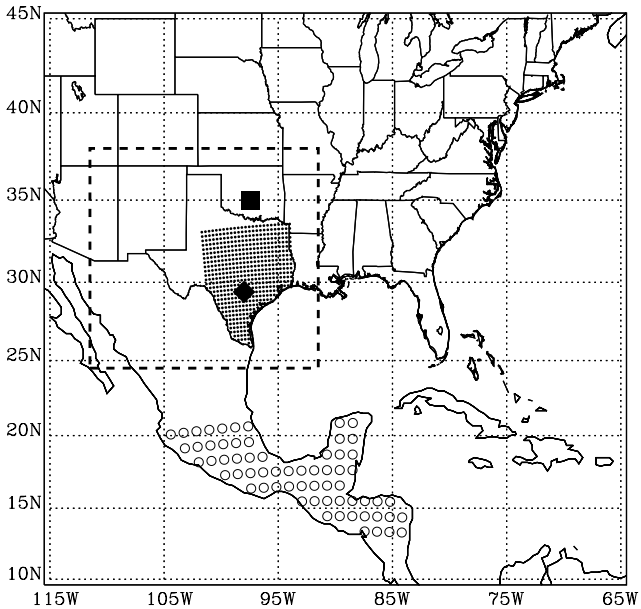

Figure 2. Model domain where the rectangle with dotted lines shows the fine-grid domain. The circles show the center of each coarse grid in the smoke source region. The dots in Texas show the center of each fine grid in the southeastern Texas. The solid square and diamond show the location of Atmospheric Radiation Measurements at Southern Great Plains (ARM SGP site) and temperature monitoring stations (Table 1) at the San Antonio area, respectively. See text for details.

[13] The NCEP/NCAR reanalysis data [*Kalnay et al.*, 1996] are used to initialize the model and further provide out-boundary conditions four times a day at 0000, 0600, 1200, and 1800 UTC, respectively. Two experiments with and without considering the aerosol radiative impacts (hereinafter SMKRAD and NSMKRAD, respectively) are conducted. In each experiment, the smoke source function is updated hourly based upon an hourly smoke emission inventory from the Fire Locating and Modeling of Burning Emissions (FLAMBE) geostationary satellite database [*Reid et al.*, 2004] which utilizes the GOES Wildfire Automated Biomass Burning Algorithm (WF-ABBA) fire product [*Prins et al.*, 1998]. *Wang et al.* [2006] showed that the original FLAMBE emission could underestimate the smoke emission by nearly 70%. Therefore, in this study, the original FLAMBE smoke emission inventory is scaled by a factor of 1.7 before it is assimilated into the model, which resulted in a total of 1.5 Tg of smoke particles emitted during 20 April to 21 May 2003. In summary, the only difference between the SMKRAD and NSMKRAD experiments is that SMKRAD explicitly considers the smoke radiative impacts during the simulation at each time step while NSMKRAD does not.

[14] Since AOT and DSWI are two important parameters in quantifying the smoke radiative impacts, the measured AOT and DSWI from the Atmospheric Radiation Measurement at Southern Great Plains (ARM SGP) site are used to compare against the model results. In addition, comparisons between modeled and measured 2 m air temperature (2mT) in Central Texas are also conducted to evaluate the ability of RAMS-AROMA for capturing the smoke feedbacks on 2mT (see section 3.2 for details). The ARM AOT data at the SGP site are inferred from a normal incidence multifilter radiometer (NIMFR), and have a reported uncertainty between $0.01 \sim 0.02$. Three instruments, precision spectral pyranometer (PSP), normal incidence pyrheliometer (NIP), and shaded PSP, are used routinely in the ARM SGP site to measure the total, direct and diffuse DSWI at the surface, respectively. All irradiance data are collected in 1 min interval, which is then processed to derive the clear and cloudy sky DSWI in different time intervals [*Long and Gaustad*, 2004]. In this study, we used the quality-controlled total downward DSWI data that have a temporal resolution of 15 min with an uncertainty less than 15 Wm^{-2} [*Long and Ackerman*, 2000].

[15] In addition to the ground-based measurements, AOT data retrieved from the Moderate Resolution Imaging Spectroradiometer (MODIS) are also used to compare against the model results. The MODIS instruments aboard NASA's Terra and Aqua satellites provide near daily global coverage at the local equatorial overpass time about 1030 LT and 1330 LT, respectively [*Remer et al.*, 2005]. In this study, we used the MODIS level 2 AOT product (from both Terra and Aqua) that has a spatial resolution of 10×10 km^2, and uncertainty within $\pm 0.05AOT \pm 0.03$ over the ocean and $\pm 0.20AOT \pm 0.05$ over the land [*Remer et al.*, 2005]. Recent studies [*Ichoku et al.*, 2005] also indicate that the MODIS AOT in some cases could overestimate the real AOT by 0.1–0.3 because of thin cirrus contamination. Since MODIS AOT is a columnar quantity that has limited information about the aerosol chemical composition and aerosol vertical distribution, a direct comparison between MODIS AOT and modeled smoke AOT is not straightforward, in particular when there are other types of aerosols in the atmospheric column. However, over the ocean when background (sea salt) AOT is low, MODIS AOT is still expected to be a good indicator of smoke AOT during the smoke episodes. Unfortunately, we found that the Gulf of Mexico is always under the sun glint influence during the MODIS over pass time [*Wang*, 2005]. This hampers us to conduct a direct paired comparison between modeled smoke AOT and MODIS AOT over the ocean. Instead, similar to previous studies [*Colarco et al.*, 2004], we qualitatively use MODIS AOT products to evaluate if the AOT distribution simulated from RAMS-AROMA is consistent in large scale with those derived from MODIS AOTs. Over the ARM site where "true" AOT is available from the NIMFR instrument, quantitative comparisons among the modeled smoke AOT, MODIS AOT and NIMFR AOT are conducted.

3. Results

[16] Comparisons of model-simulated smoke AOT, DSWI at the surface, and 2mT with the corresponding ground-based observations are first presented (sections 3.1 and 3.2). The comparison focuses on the smoke event on 8 May 2003, when all measurements and meteorological data sets are available (e.g., in cloud-free condition). It should be noted that all model quantities are an averaged values in 30×30 km^2 grid, while the measured data are only representative at the ground-observation site and therefore some discrepancies are to be expected. After the comparison, we present geographically the change of surface energy budget (section 3.3), air temperature, and other boundary layer processes (section 3.4) caused by the smoke radiative impacts, mainly from a monthly mean perspective. A quantitative analysis of these results in both the smoke source region and downwind region is carried out in section 3.5. The radiative feedbacks and implication of these results for the air quality modeling are then discussed in section 3.6.

3.1. Comparison of AOTs and DSWI

[17] Figure 3 shows the time series of model-simulated smoke AOT and its comparison with NIMFR AOT and MODIS AOT at ARM SGP site. Since long-term observations have shown that the background AOT at the ARM site is about 0.1 at 0.55 μm [*Michalsky et al.*, 2001], we have added 0.1 to the modeled smoke AOT in Figure 3. In general, the model captures the variations of NIMFR AOT very well. In particular, for two smoke events during 9–12 May and 14–17 May, the NIMFR AOT showed significant variations. In both time periods, the NIMFR AOT continuously increased and reached their peaks about 0.4 during the smoke front passage, and slowly decreased to the background AOT value of 0.1 toward the end of smoke events. Such timelines of both smoke events are well simulated by the RAMS-AROMA, if we consider that the model run starts on 20 April 2005, and the ARM site is about more than ~1800 km away from the smoke source in Yucatan Peninsula. The difference between the model-simulated and NIMFR-indicated smoke intrusion time (the time when smoke AOT starts to increase) and smoke ending time (the time when smoke AOT decreases to the background AOT) is only within 2–5 hours. Note that the

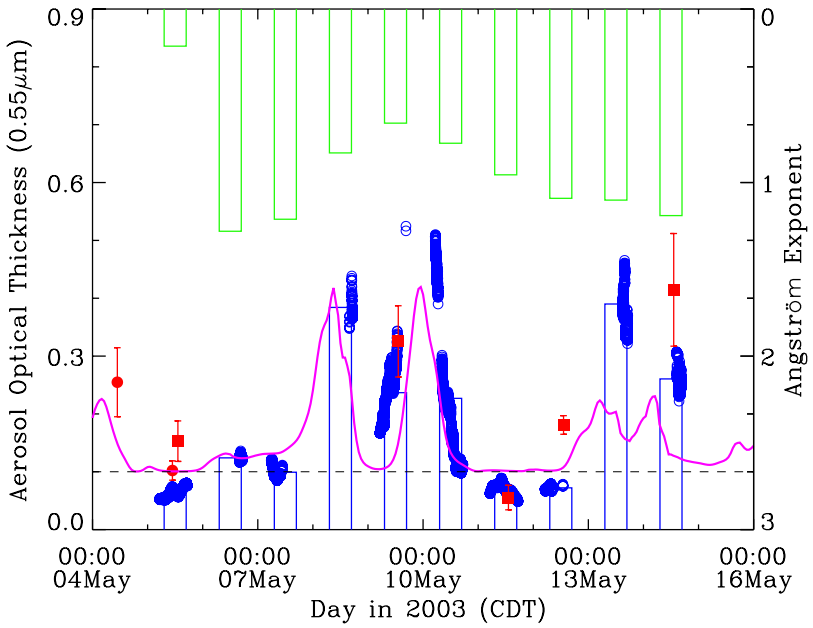

Figure 3. Time series (in CDT, Central Daylight Time) of NIFMR-measured AOT (blue dots), MODIS AOT from Terra (red dots) and Aqua (red squares) and modeled smoke AOT (pink line) at the ARM SGP site. Bars in blue and green show the daily averaged AOT and Angstrom exponents derived from the NIMFR AOT, respectively. The MODIS AOT values and their error bars are reported, respectively, as the mean and ±1 standard deviation of 3X3 MODIS AOT retrievals centered at the ARM SGP site. Note that to compensate the lack of background AOT in the model, all modeled smoke AOT have been added 0.1 (dashed line).

Angstrom exponents decreased during the smoke events (Figure 3), which is consistent with the results of *Andrews et al.* [2004] who used 2 years of ARM data sets and showed that long-range transported smoke aerosols usually result in the decrease of the Angstrom exponent at the ARM site. Quantitatively, the modeled smoke AOT is smaller than NIMFR AOT, even after the background AOT is taken into account since there are other aerosols such as sulfate that were being transported to the ARM site along with the smoke plumes [*Wang et al.*, 2006]. In addition, because NIMFR AOTs only represent the AOTs at the observation point, the difference between the modeled and measured AOT could also be due to the inability of the current RAMS-AROMA to resolve the nonhomogeneity smoke distribution in the 30×30 km^2 grid.

[18] Similarly, a reasonable agreement can be found between the modeled smoke AOT and the MODIS AOT, except on 14 May where the MODIS AOT seems to be much higher than modeled smoke AOT. The large spatial variations (standard deviation bar) of MODIS AOT around the AMR SGP site indicate a possible cloud contamination in the MODIS AOT retrieval on that day. More interestingly, on 14 May when there are no valid MODIS AOT retrievals, implying at least partially cloudy conditions over the ARM site. The NIFMR on the other hand showed high AOTs, implying clear sky conditions at the NIFMR site. This demonstrates that the air mass is very inhomogeneous on 14 May; another possible reason for the large difference between modeled and NIFMR AOT. Nevertheless, although only a few MODIS AOT points (7 out of 20 days) are available at the ARM SGP site during the study period, their reasonable agreement with modeled smoke AOT is encouraging because MODIS AOT are grid (not point) quantities. The general consistency of modeled smoke AOT with the MODIS AOT and NIMFR AOT provides the basis for computing the smoke radiative impacts realistically in RAMS-AROMA.

[19] Figure 4 shows the comparison of DSWI at surface at the ARM SGP site on 8 May, 2003. The daytime averages of the modeled smoke AOT on this day is the largest during the study time period, thus facilitating us to illustrate the smoke radiative impacts on DSWI. The diurnal variation of DSWI is well simulated in both SMKRAD and NSMKRAD cases (Figure 4a). Because the radiative extinction of atmospheric smoke layers attenuates the solar radiation, less DSWI is expected to reach the surface during the smoke events such as on 8 May. This is the reason that the DSWI in NSMDRAD case is consistently larger than the measured DSWI and SMKRAD-simulated DSWI. The SMKRAD also overestimates the measured DSWI, possibly because the scattering of background aerosols (of AOT about 0.1 and other type of aerosols associated with smoke plumes) has not been incorporated in the radiative transfer calculations. Depending on the solar zenith angle and smoke AOT values, the simulated DSWI in NSWKRAD case overestimate the measured DSWI by 25–65 Wm^{-2}, larger than the overestimation of 0–40 Wm^{-2} in SMKRAD case (Figure 4b). Overall, SMKRAD gives a better agreement with the measured DSWI, particularly during high smoke AOT conditions (e.g., morning to early afternoon on 8 May). The difference in DSWI between NSMKRAD and SMKRAD cases is about 20 Wm^{-2} on 8 May. This

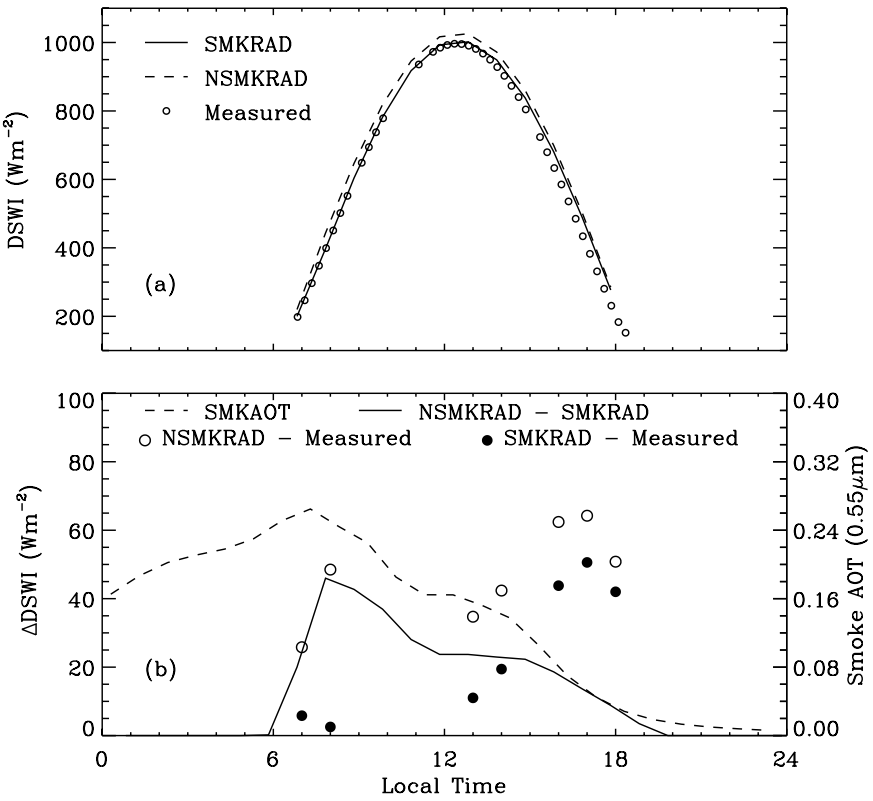

Figure 4. (a) Diurnal variation of modeled and measured downward shortwave irradiance (DSWI) at the surface at the ARM SGP site on 8 May 2003. The modeled DSWI are reported from two model experiments with (solid line) and without (dotted line) considering smoke radiative effects (e.g., SMKRAD and NSMKRAD), respectively. (b) Difference between measured and modeled DSWI (ΔDSWI) at the surface in SMKRAD (solid circles) and NSMKRAD (open circles), respectively. Also shown are the modeled smoke AOT (dotted line) and the difference of DSWI between SMKRAD and NSMKRAD cases (e.g., NSMKRAD ∼ SMKARD, solid line). Note that modeled DSWI and AOT values are reported on an hourly basis.

difference is expected to be much larger in the smoke source region, since the smoke AOT is usually (2–5 times) smaller at the ARM SGP site than in the source region or even the southern Texas. Unfortunately, the lack of ground-based irradiance measurements along the smoke path way (from the Yucatan Peninsula to southern Texas) hampers us to conduct more comparisons.

3.2. Comparison of 2mT

[20] The accurate prediction of surface air temperature depends on many factors including the realistic representation of dynamical and thermodynamic processes, the accurate description of land surface processes, and the reliable parameterization of turbulent processes in PBL. A better estimation of surface energy input can therefore improve the modeling of surface energy budget and in turn the air temperature near the surface. This postulation is evaluated by comparing the RAMS-AROMA simulated 2 m air temperature (2mT) with the measured 2mT in San Antonio, Texas. We selected the San Antonio region as the focus region for several reasons. First, it is located in the southern part of Central Texas (Figure 2) where the mass concentration of transported smoke particles is larger than those in northern Texas [*Wang et al.*, 2006]. This makes the impact of smoke layers on the 2mT in this region more distinguishable. Secondly, in the San Antonio region, there are 4 meteorological stations (see Table 1) from which the averaged 2mT in this region can be better inferred than from a single station alone. This advantage facilitates the comparison with the modeled 2mT values that are averaged quantities over each 30×30 km^2 grid. Thirdly, the San Antonio region is far away from the coast of Gulf of Mexico and sea breeze has negligible impact on 2mT in this region. In summary, we conduct the comparison between model and observation in an optimal situation so that the smoke radiative impacts on 2mT can be favorably identified.

[21] Figure 5 shows the comparison between modeled and measured 2mT in San Antonio, Texas, on 8 May 2003. On this day, the modeled smoke AOT in San Antonio is about 0.35 (figure not shown). Two model grids cover the San Antonio region, and there are two meteorological stations collocated within each grid. In either grid (Figures 5a and 5b), the simulations from SMKRAD and NSMRAD cases demonstrate a consistent diurnal temperature pattern with those from observations. Quantitatively, the modeled 2mT in SMKRAD case is about 0.3°C smaller than that in NSMKRAD case, because smoke radiative

Table 1. Location of Four Meteorological Stations That Measure the Hourly 2 m Air Temperature in San Antonio, Texas

Meteorology Station	Latitude	Longitude
1	29.5150	−98.6200
2	29.4444	−98.4056
3	29.6322	−98.3117
4	29.2752	−98.3117

extinction blocks the solar radiation from reaching the surface. SMKRAD gives a better agreement with observations, particularly during late morning to local afternoon when smoke radiative impacts are pronounced. In Figure 5a, the NSMKRAD overestimates 2mT by 0.8°C, while SMKRAD virtually has no bias with observation. In Figure 5b, the 2mT at local noon is overestimated by more than 1.0°C in the NSMKRAD case, while SMKRAD shows a reasonable agreement with observations. In later afternoon (1600–2000 LT), the measured 2mT at 4 stations showed relatively large differences (Figures 5a and 5b), which could be due to the presence of broken clouds (as judged from the geostationary satellite GOES images). As a result, during this time period, the modeled 2mT showed relatively larger bias in both grids, because the radiative impacts of broken clouds in the subgrid scale cannot be resolved well by the cumulus parameterization used in the model. It is also interesting to note that these particular hours were also the time period when modeled and measured DSWI showed the largest difference (Figure 4b). Thus the difference could also be possible because of a large-scale concurrent disturbance that was not well captured by the model. However, our limited intercomparisons suggested that the consideration of the smoke radiative impacts (e.g., SMKRAD experiment) is necessary for simulating the 2mT accurately.

3.3. Large-Scale AOT Distribution and Its Impact on Surface Energy Budget

[22] *Yu et al.* [2002] showed that for an aerosol layer with a fixed single scattering albedo, its impact on the surface energy budget is highly relevant to AOT values. In this section, the large-scale comparison between model-simulated AOT and MODIS AOT is first conducted before the smoke radiative effect in smoke source region and downwind region are examined. Figure 6b shows the distribution of mean AOT averaged over 24 hours for a total of 30 days from 20 April to 20 May 2003 (hereinafter 30-day 24-hour averages). It reveals two AOT maximum centers, one in the Yucatan Peninsula, and another in the Manzanillo region (103°W, 18°N) along the Pacific Ocean coast. The locations of these two centers are consistent with regions that have intensive fires and hence high smoke emissions [*Wang et al.*, 2006]. In contrast to the smoke particles from burning in the Yucatan Peninsula, which can be continuously transported along the Gulf of Mexico coast and reach the U.S. under the influence of southern flow, smoke plumes from the Manzanillo region seldom reach western Texas because of the high mountains along their transport path. The smoke plumes from this region are mainly transported to the Pacific Ocean under the favorable easterly flow (Figure 6b) [see also *Rogers and Bowman*, 2001].

[23] The above AOT distribution and smoke transport pattern can also be identified from the 30-day averaged MODIS AOT image (Figure 6a). Although the instantaneous MODIS AOT and the modeled smoke AOT are in reasonable agreement (Figure 3) at the ARM SGP site, interpretation of Figure 6a versus Figure 6b should be done cautiously. First, MODIS AOT includes not only smoke AOT, but also AOT of other types of aerosols. Thus MODIS AOT should be always larger than the modeled smoke AOT. Secondly, the sampling of AOT by MODIS is only twice a day in maximum, one from Terra (1030 LT) and one from the Aqua (1330 LT) satellite. In addition, MODIS AOT is also not available in cloudy and sunglint regions. These limitations pose a challenge for computing the climatological statistics from MODIS AOT, which requires adequate data for temporal and spatial averages. In this study, we segment the study domain into $1 \times 1^\circ$ grid. For each grid, two methods are used to calculate the 30-day averaged AOT value. One is to compute the daily mean, and then compute the 30-day mean from daily values. Another is to compute

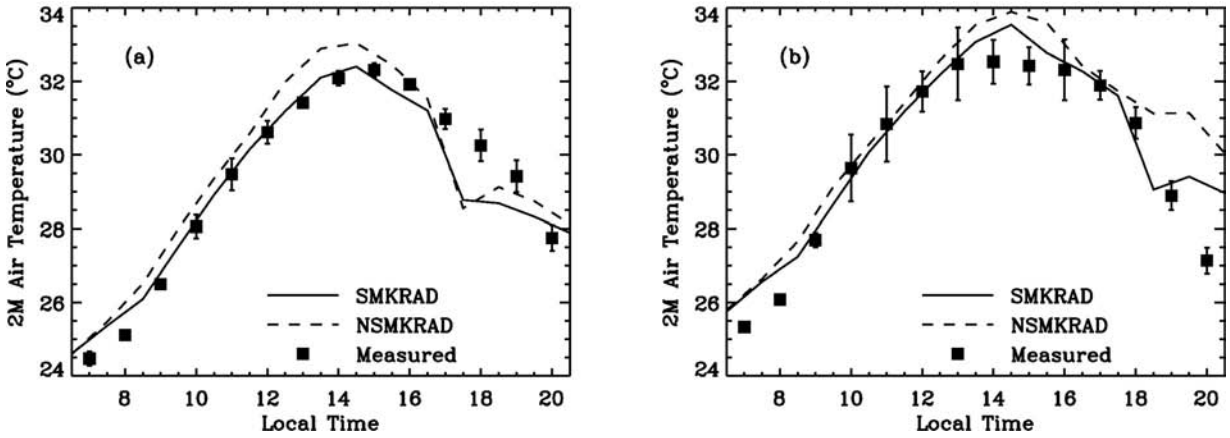

Figure 5. (a and b) Two-meter air temperature in daytime on 8 May 2003 in two model 30×30 km^2 grids at San Antonio. In each panel, solid squares and their error bars are the mean and ±1 standard deviation of temperature data reported at two different stations corresponding to that model grid. Solid and dotted lines represent the modeled temperature with and without considering smoke radiative effects (e.g., in SMKARD and NSMKRAD cases), respectively.

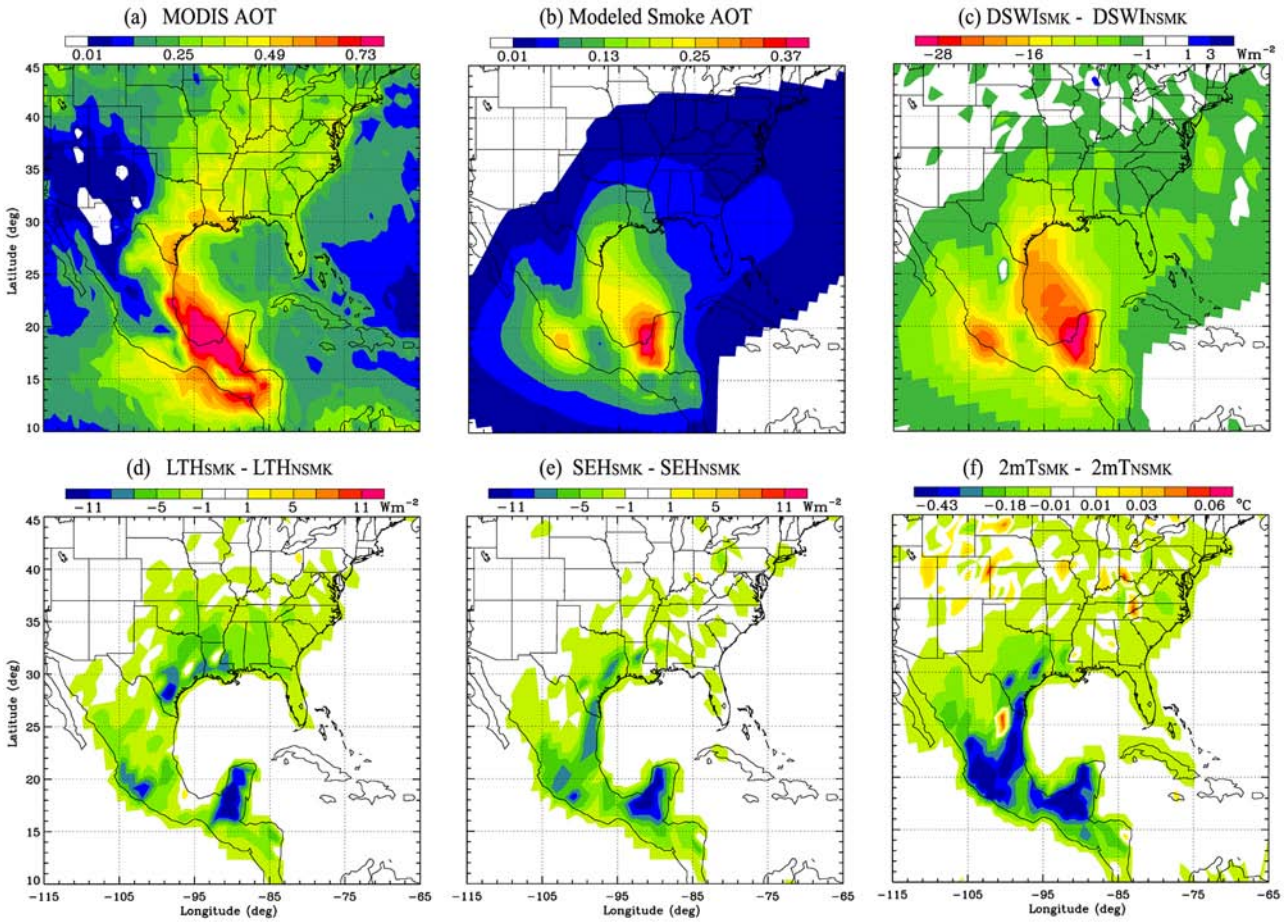

Figure 6. Distribution of averaged quantities during 20 April to 20 May 2003. (a) MODIS AOT. (b) Smoke AOT in SMKRAD simulation. (c–f) Difference between SMKRAD and NSMKRAD simulations of DSWI, latent heat (LTH), sensible heat (SEH), and 2 m air temperature (2mT) at the surface, respectively. For model variables in Figures 6b–6f, averages are conducted in both day and night. See details in the text about averaging of MODIS AOT.

the mean of all available AOT data in that grid for 30 days. The two methods can give a difference about 0.1–0.2 in the smoke source region [*Wang*, 2005]. Besides the averaging methods, the statistics are also questionable in those regions that have large cloud fraction or are frequently influenced by sunglint. Other factors including the MODIS instantaneous AOT uncertainties (0.20 AOT ± 0.05 over land and 0.05 AOT ± 0.03 over ocean) and nonidealities in RAMS-AROMA simulation (e.g., about 20% underestimation of smoke extinction efficiency, [*Wang et al.*, 2006]) could result in large differences between modeled smoke AOT and MODIS AOT. *Chin et al.* [2004] found that the CTM-simulated AOT (that includes all major types of aerosols) is about 2–3 factors lower that MODIS AOT in tropical biomass-burning region such as Central America. Similarly, *Reid et al.* [2004] argued that cloud contamination can result in an overestimation of 0.1 in the MODIS AOT. This overestimation plus the background AOT (at least 0.1 in Mexico) can together result in the AOT difference of at least 0.2 between MODIS AOT and their model-simulated AOT that does not consider the background aerosols [*Reid et al.*, 2004]. Recently, *Remer et al.* [2005] showed that a difference of ±0.2 between MODIS monthly AOT and ground-based Sunphotometer inferred monthly AOT is also possible over several locations. While considerable differences (a factor of 2 in smoke source region) were found between MODIS AOT (Figure 6a) and RAMS-AROMA AOT (Figure 6b), these differences are still within the aforementioned MODIS AOT and modeled AOT uncertainties as well as the discrepancies reported in the literature. Although a full reconciliation of the MODIS and modeled AOT difference is out the scope of our current study, we found that the MODIS AOT map (Figure 6a) and modeled smoke AOT map (Figure 6b) are still in qualitative agreement in description of smoke transport path, i.e., both indicating high AOT along east and west coast in Mexico, and low AOT in the Mexico Central Plateau that is surrounded by the Sierra Madre Mountains.

[24] The reduction of DSWI near the surface caused by smoke radiative impacts has a consistent pattern with modeled smoke AOT. The surface radiative energy input (DSWI) is reduced by ~20–30 Wm^{-2} in the smoke source region, and by ~5–10 Wm^{-2} and ~1–5 Wm^{-2} in the southern part of Texas, and other southern states along the coast of Mexican Gulf, respectively (Figure 6c). As a result, both latent heat (LTH) and sensible heat (SEH) are decreased by ~8–10 Wm^{-2} in the smoke source region in Yucatan Peninsula, and about 1–5 Wm^{-2} in the coastal area

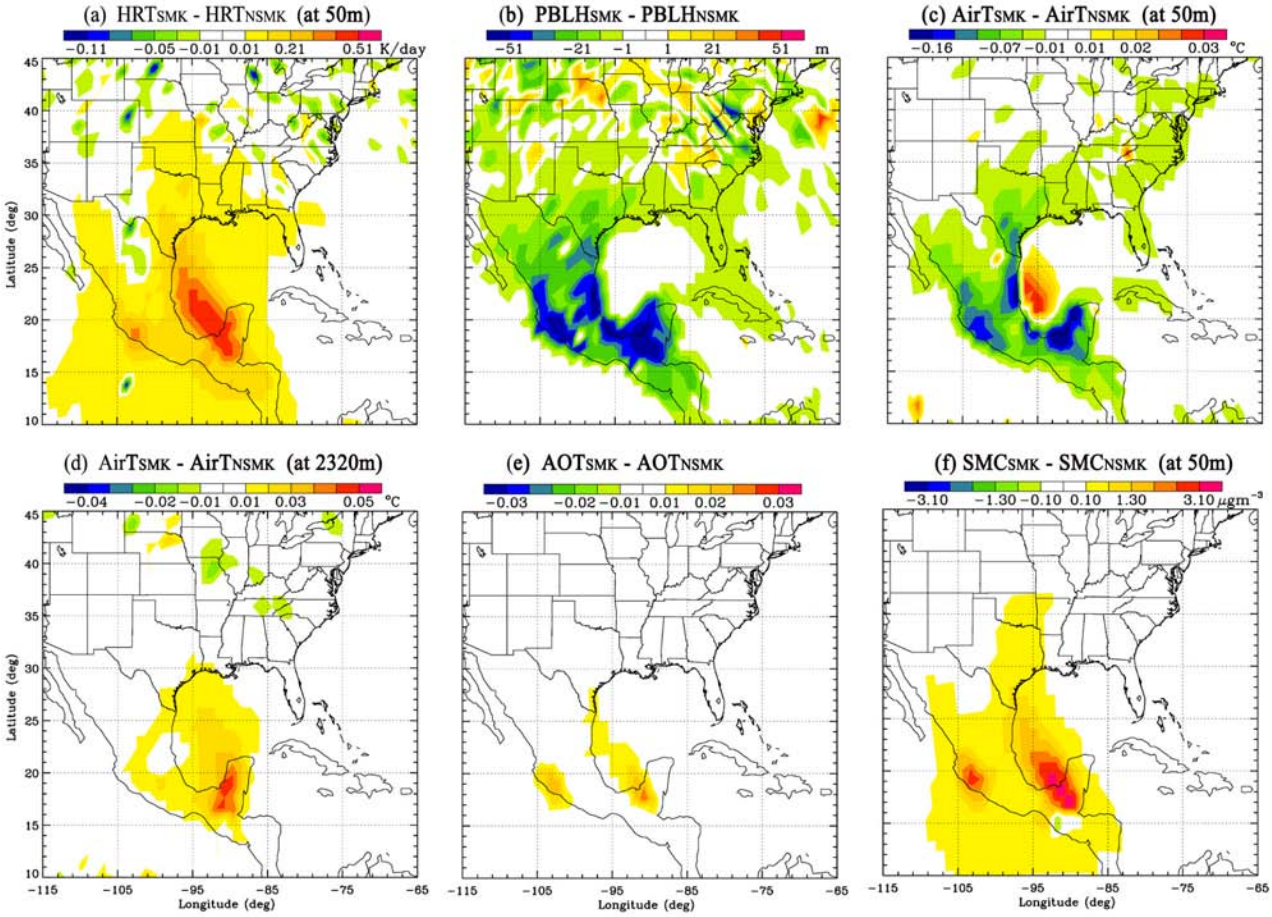

Figure 7. Similar to Figure 6c but for the difference of (a) atmospheric heating rate (HRT), (b) plenary boundary layer height (PBLH), (c) temperature (T) in the first model layer (about 50 m) above the surface, (d) T in the ninth model layer (about 2320 m) above the surface, (e) AOT, and (f) smoke mass concentration (SMC) in the first model layer above the surface.

of Mexican Gulf. The difference in the changes of LTH and SEH (shown in Figures 6d and 6e) in different regions reflects their dependences on the surface albedo and the surface type. For a mesoscale meteorological model like RAMS, the temperature over the land is usually simulated by a multilayer land surface model (e.g., RAMS LEAF model) in which the processes involved in the surface energy budget over various vegetation and soil types are sophisticatedly described [*Walko et al.*, 1995]. However, over the ocean, only a simplified one layer model is used in which sea surface temperature (SST) is diagnosed as the climatological ocean surface temperature values. While this simplification is not perfect, it is physically meaningful and convenient in the mesoscale models, because daily or even monthly variation of SST is normally small. Consequently, it is reasonable that the smoke radiatively induced changes of SEH and LTH are not significant over the ocean (Figures 6d and 6e).

[25] The 2mT difference caused by the smoke radiative impacts is shown in Figure 6f. Because of the reduction of DSWI at the surface, 2mT is decreased by ∼0.2°–0.4°C in regions that have high smoke AOTs, and by ∼0.05°–0.2°C in low AOT regions such as the southeastern United. It should be emphasized the 2mT depends on various factors, not only surface energy budget, but also the temperature advection. Thus it is not unreasonable to see several small regions where 2mT is increased, possibly because of the advection of warmer air caused by the smoke radiative absorption (section 3.4).

3.4. Smoke Radiative Impacts on PBL Process

[26] While smoke radiative impact on the surface energy budget originates mainly from its extinction on the DSWI, smoke layers absorb the solar radiation and increase the atmospheric heating rate (HRT). The increase of HRT in turn depends on the smoke vertical distribution. Figure 7a shows the distribution of 30-day 24-hour averaged HRT in the model first layer, indicating an increase of 0.4–0.5 K/day can be found in high AOT regions as Yucatan Peninsula and the near-Mexico-coast ocean areas in Gulf of Mexico. In contrast, the increase of HRT in moderate AOT regions such as southern Texas is about 0.2 K/day.

[27] The overall response of air temperature to the smoke radiative heating in the atmosphere and radiative cooling near the surface depends highly on the surface characteristics as well as the aerosol vertical profile. Over land, the turbulent mixing in lower PBL is efficient in transporting heat between the atmosphere and surface. As a result, the response of the air temperature (AirT) to smoke radiative impacts relies on two competing processes, e.g., an increase

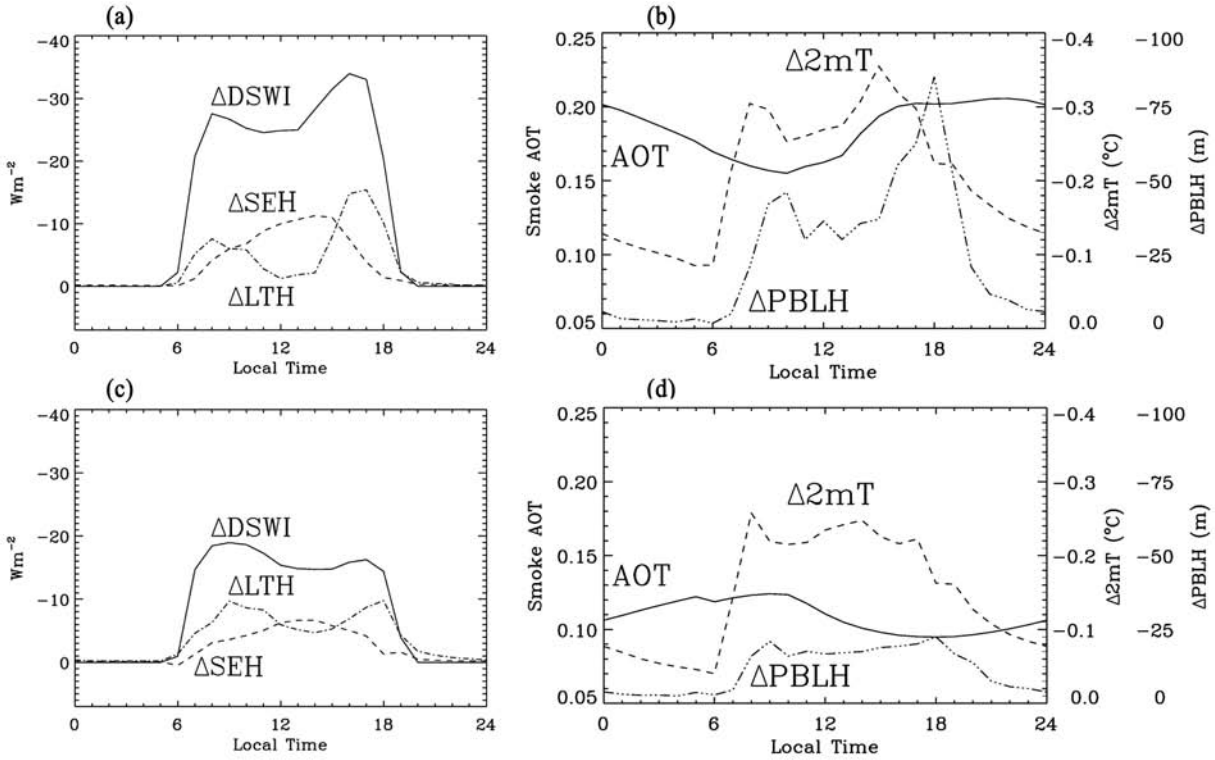

Figure 8. Monthly averaged and area-averaged diurnal change of smoke aerosol optical thickness (AOT) as well as smoke-radiative-effect-caused differences of downward shortwave irradiance (ΔDSWI), sensible heat (ΔSEH), latent heat (ΔLTH), planetary boundary layer height (ΔPBLH), and 2 m air temperature (2mT) in (a and b) smoke source region and (c and d) downwind southeastern Texas.

of AirT due to the increase of HRT, a decrease of AirT due to the cooler surface and thus weaker turbulent transfer of heat from the surface. In atmospheric layers near the surface, the coupling between surface and air processes is strongest. Therefore the impact of cooler surface on AirT could outweigh the impacts of smoke radiative heating. Model results showed that the AirT in the first layer of model is cooled by $\sim$0.1°–0.15°C in the high AOT regions in Mexico, while AirT in the downwind regions (such as in states of Mississippi and Louisiana) is only decreased by 0.01°C to 0.06°C (Figure 7c). On the contrary, in the altitude near or above the top of boundary layers where the turbulent mixing becomes weaker and the surface starts to have less influence on the atmospheric processes, the increase of HRT by the smoke absorption begin to play a dominant role. The AirT in the model's 8th layer (about 2320 m) was increased by $\sim$0.02°–0.05°C in high AOT regions (Figure 7d). The dependence of smoke radiative impact on the smoke vertical profile is further discussed in detail in section 3.5.

[28] Over the ocean, because of its large heat capacity and increased depth of the mixing layer, the SST changes due to the reduction of DSWI in magnitude of $\sim$10–20 Wm^{-2} can be considered negligible, at least in a 30-day timescale. Thus the smoke radiative impacts on the ocean surface temperature and in turn on the turbulent mixing are less significant. Consequently, the air above the ocean is warmer in all layers in which HRT is increased by smoke absorption. This is verified by the model results shown in Figures 7c and 7d. Although a direct validation of such warming is hampered by the lack of data over the ocean, we found that such smoke-induced warming is similar to the finding of *Alpert et al.* [1998] who showed that the GCM-simulated air temperature in the lower troposphere (1.5–3.5 km) over the eastern tropical Atlantic ocean always had a negative bias when compared to the reanalysis results (an optimal blending of observation and model simulation), and the distribution of such negative bias bear a striking similarity with the observed pattern of Saharan dust over this region. They attributed this negative bias to the lack of consideration of dust absorption of solar radiation in the GCM, which can enhance the atmospheric heating by 0.2 K/day during normal dust days, consistent with our findings in Figures 7a and 7c.

[29] The smoke radiative impacts on the turbulent mixing and air temperature would also affect the evolution of boundary layer [*Yu et al.*, 2002]. While there are no widely accepted methods for quantitatively defining PBLH [*Seibert et al.*, 2000], RAMS calculates the PBLH on the basis of the turbulent kinetic energy (TKE) and assumed that the PBL height is the lowest altitude where the TKE is less than a threshold value. Figure 7b showed the mean difference of PBLH in 30 days with and without considering aerosol radiative impacts. Decrease of PBLH from $\sim$20–50 m can be found in the smoke source regions and the southern part of Texas.

3.5. Quantitative Summary in Source and Downwind Regions

[30] Figure 8 provides the diurnal variations (values at each hour are 30-day averages in that hour) of AOT, and

Table 2. Change of Surface Energy Budget Caused by Smoke Aerosols in the Smoke Source Region and Downwind Regions[a]

	AOT	ΔDSWI, Wm^{-2}	ΔLTH, Wm^{-2}	ΔSEH,Wm^{-2}	Δ2mT, °C	ΔPBLH, m	ΔMin2mT, °C	ΔMax2mT, °C
Source region								
Daytime average	0.18	−22.5	−6.2	−6.2	−0.28	−41	−0.15	−0.46
24-hour average	0.18	−11.8	−3.1	−3.1	−0.21	−25	−0.15	−0.46
Downwind region								
Daytime average	0.10	−15.8	−7.9	−4.7	−0.20	−17.2	−0.05	−0.31
24-hour average	0.10	−7.9	−3.8	−2.8	−0.15	−11.6	−0.05	−0.31

[a]See text for the meanings of each acronym.

changes of PBLH, 2mT, SEH, LTH, and DSWI due to the smoke radiative impacts (hereinafter ΔPBLH, Δ2mT, ΔSEH, ΔLTH, and ΔDSWI) in smoke source regions (Figures 8a and 8b) and downward regions (in southern Texas, Figures 8c and 8d). The daytime (12-hour) average and all day (24-hour) average of these quantities are summarized in Table 2. Except AOT that shows about ±12% changes between day and night, other quantities are mostly pronounced during the daytime. Hereinafter in the following analysis, all the averages are daytime averages.

[31] Results indicate that smoke AOT is about 0.18 in the source region, and decreases to 0.09 in the downwind region. The area-averaged AOT has a distinct diurnal variation of 24% (±12% from the mean) but opposite patterns in smoke source region and the downwind regions. In source region, Figure 8b showed that the largest AOT occurs in the early afternoon (1500∼1600 LT) while minimum AOT is in the morning (0800∼0900 LT), consistent with previous findings from satellite observations [*Prins et al.*, 1998] and ground-based observation [*Eck et al.*, 2003]. In contrast, AOT in downwind regions has maximum (minimum) value in the morning (early afternoon). The mechanism for this opposite diurnal variation pattern is not clear, although the smoke transport time from the source to Texas could shift the phase of diurnal variation.

[32] Consistent with AOT diurnal variations, DSWI in smoke source region is larger during the afternoon than in the morning, contrary to that in the downwind regions. In both regions, DSWI shows two peaks, one at ∼0800 LT and another is around 1600 LT. This is largely due to the solar zenith angle effect. On one hand, the total incoming solar energy at the TOA is a function of cosine of solar zenith angle, and has maximum values during local noon. On the other hand, the AOT along the slant path is enhanced by the cosine of solar zenith angle, which means that the actual AOT that attenuates the sunlight reaches maximum values near the sun set. Because of these two competing factors, ΔDSWI at the surface induced by the same AOT reaches the maximum value when solar zenith angle is around 60° [*Christopher et al.*, 2003; *Russell et al.*, 1997]. In daytime (12-hour) average, the DSWI at the surface is decreased by 22.5 Wm^{-2} in the smoke source region, and 15.8 Wm^{-2} in the downwind regions.

[33] Compared to ΔDSWI, the change of latent heat (ΔLTH) shows similar patterns but smaller values. During the tropical dry season, the relative humidity near the surface in the smoke source region is lower than that in the smoke downwind region. As a consequence, the impact of ΔDSWI on the ΔLTH is larger in smoke downwind region. About half of ΔDSWI goes to the ΔLTH in the downwind southern Texas regions, while in the smoke source region, that ratio is about 0.3 (Table 2). Indeed, ΔLTH is decreased by about 1.7 Wm^{-2} larger in downwind regions. On the other hand, ΔSEH mainly relies on the difference of air temperature and surface temperature, and therefore its diurnal pattern to some extent should follow the variations of diurnal temperature. In daytime averages, ΔSEH is about −6.2 Wm^{-2} and −4.7 Wm^{-2} in smoke source and downwind regions, respectively, both showing maximum in the early afternoon time (1300−1500 LT, Figures 8a and 8c).

[34] The surface energy budget is balanced by the ΔDSWI, ΔLTH, and ΔSEH as well as the change of longwave (LW) radiation or temperature at the surface. Figures 8b and 8d showed that the Δ2mT has a similar diurnal variation to ΔDSWI with dual peaks in the early morning and late afternoon, implying that the change of LW is closely responded to the ΔDSWI in order to achieve a surface energy balance. They also showed that the atmospheric response to the aerosol radiative impacts has a distinct diurnal cycle. Depending on the solar zenith angles, the maximum decrease of 2mT can be as high as 0.35°C and 0.28°C in smoke source and downwind regions, respectively. On an average, Δ2mT is decreased by 0.28°C near the source, and about 0.20°C in the downwind region. Because the decrease of 2mT is much larger in the daytime than in night time, it is expected that the DTR (maximum 2mT − minimum 2mT) is reduced by the smoke radiative effects. Our calculation showed that maximum 2mT and minimum 2mT are reduced respectively by 0.46°C and 0.15°C in the smoke source region, larger than 0.31°C and 0.05°C in the down region (Table 2). Overall, DTR is reduced by 0.31°C and 0.26°C in the smoke source region and southern Texas, respectively.

[35] The diurnal variation of ΔPBLH has a one to two hour lag behind the temporal variations of ΔDSWI and Δ2mT (Figures 8b and 8d). This is because the response of ΔPBLH to the decrease of 2mT involves the turbulent mixing process in the boundary layer. Thus the impact of the decreased heat flux can only be reflected 1∼2 hours later on the change of ΔPBLH. In average, the ΔPBLH is about −41 m in the source and −17.2 m in the downwind regions (Table 2). Previous studies [*Yu et al.*, 2002; *Feingold et al.*, 2005] showed that for the same amount of AOT, the aerosol radiative effect on the PBLH also highly depends on the aerosol single scattering albedo (SSA) and the aerosol vertical distribution. For the moderately absorbing aerosols with SSA of 0.9 (the value used in this study), the PBLH is slightly decreased when the aerosol layer is in the lower PBL (e.g., within 1 km), and can be significantly decreased if the aerosols layer is above the PBL [*Yu et al.*, 2002]. However, for strong absorbing

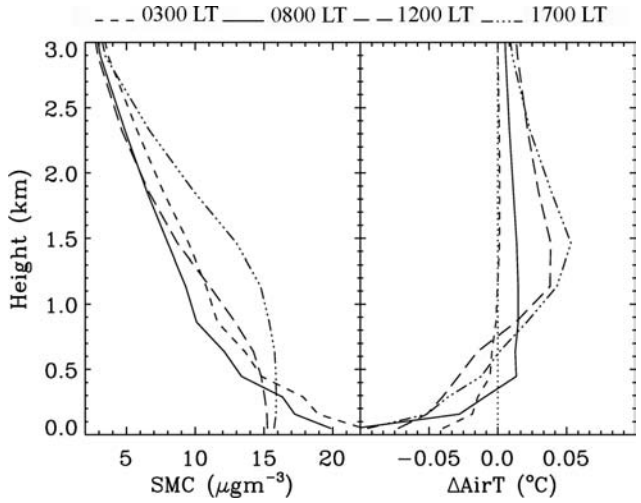

Figure 9. Vertical distribution of (left) smoke mass concentration (SMC) in SMKRAD case and (right) the smoke-radiative-effect-caused difference of air temperature ($\Delta AirT = AirT_{SMKRAD} - AirT_{NSMKRAD}$) averaged in the smoke source region in 30 days for four different local time periods (short-dashed line, 0300 LT; solid line, 0800 LT, long-dashed line, local noon; and dot-dashed line, 1700 LT). The profile of $\Delta AirT = 0$ is shown as dotted line.

aerosols (SSA = 0.8), PBLH is indeed increased when the aerosol layer is within 1 km above the surface [*Yu et al.*, 2002]. It is important to note that these studies generally assumed a well-mixed and time-independent aerosol profile in their simulations, hence caution must be exercised to compare these studies with our simulations in which the smoke profiles are modeled at each time step and are amendable to the influence of diurnal variation of fire emission, ambient meteorological condition and the large-scale synoptic systems.

[36] For instance, during local morning (say 0300 LT or 0800 LT), the smoke mass is mainly located near the surface in the shallow boundary layer, and decreases rapidly with height (Figure 9), because the fire emission is minimal and turbulence mixing is weak during this time period. However, as the time progresses, the stronger turbulence mixing together with the increased fire activities start to build up a well-mixed smoke distribution, first within about 500 m in local noon, and then within more than 1 km at 1700 LT (Figure 9). As such, the column burden of smoke mass increases rapidly after the fire activity starts in the late morning and achieves maximum values in the later afternoon, but the surface smoke concentration has the maximum in the night. Consequently, during the night (e.g., 0300 LT), the air temperature differences between SMKRAD and NSMKRAD simulations ($\Delta AirT$) is negative with small magnitude and only appears near the surface (Figure 9), because this difference is due to the residual effect of $\Delta AirT$ in the daytime. As the sun rises (at 0800 LT), the $\Delta AirT$ starts to increase (e.g., more negative or cooler) near the surface, but become positive (e.g., warming) above the PBL, consistent with *Yu et al* [2002]. During the local noon and later afternoon, this warming continues to increase in the upper PBLH, and as PBL increases, the layer with the maximum warming also grows upward (Figure 9). In contrast, the cooling (negative $\Delta AirT$) continues to remain nearly constant in the lower PBL. The critical layer at which the $\Delta AirT$ shifts from negative to positive is near 200 m during the night, and increases to 700 m at 0500 LT. Such smoke feedbacks on temperature profile enhance the atmospheric stability in the PBL, and as a result, more smoke mass will be trapped near the surface in SMKRAD case than that in NSMKRAD case. Although this overall smoke impact on PBLH showed in our simulation is consistent with *Yu et al* [2002], we learned from Figure 9 that the smoke vertical profile (both shape and magnitude) can vary significantly with the PBL process and the diurnal variation of smoke emission. Hence the results from those simulations with constant and well-mixed smoke profile need to be carefully scrutinized, particularly during the eddy simulation of aerosol-cloud interactions [*Feingold et al.*, 2005].

3.6. Smoke Radiative Feedbacks and the Implications for Air Quality Studies

[37] Since the smoke radiative effects can result in measurable changes of surface energy budget and turbulent mixing in the PBL, one would expect to find differences in smoke distribution between the NSMKRAD and SMKRAD cases. Figure 7e shows that the difference of 30-day 24-hour averaged AOT in NSMKRAD and SMKRAD cases is about 0.02∼0.03 in high AOT regions, and negligible in other regions. Because AOT is a column quantity, to explain AOT differences, it is meaningful to first examine the difference of smoke mass distribution in different vertical layers (Figure 7f). The smoke mass concentration in the model first layer above the surface is higher in the SMKRAD case than in the NSMKRAD case (Figure 7f). This indicates that more smoke is trapped in the lower PBL near the surface because of the weaker turbulence mixing and lower PBLH in the SMKRAD case. Compared to NSMKRAD case, an increase of smoke concentration by $1-3$ μgm^{-3} in SMKRAD case can be found in several lower atmospheric layers (up to 800 m) over the two high smoke AOT regions (Figure 7f). In contrast, the negative difference of smoke concentration (e.g., smaller smoke concentration in the SMKRAD case) can be found in several upper atmospheric layers (800–2000 m, figures not shown). This is because of weaker turbulent mixing in the SMKRAD that is less efficient in transporting smoke particles to the upper levels. In summary, the AOT and smoke concentration differences in the SMKRAD and NSMKRAD cases are measurable and presumably, results from SMKRAD should be more representative of real atmosphere, since SMKRAD incorporates more complete physics (e.g., smoke radiative impacts). However, the validation of this conclusion is still difficult because of the lack of accurate chemical speciation measurements in the study region. Since relative humidity is usually higher in the lower PBL than in upper PBL, hygroscopic effect is more pronounced in the lower PBL. For the same amount of smoke mass, larger AOT would be expected if more smoke is located in the lower PBL (than in

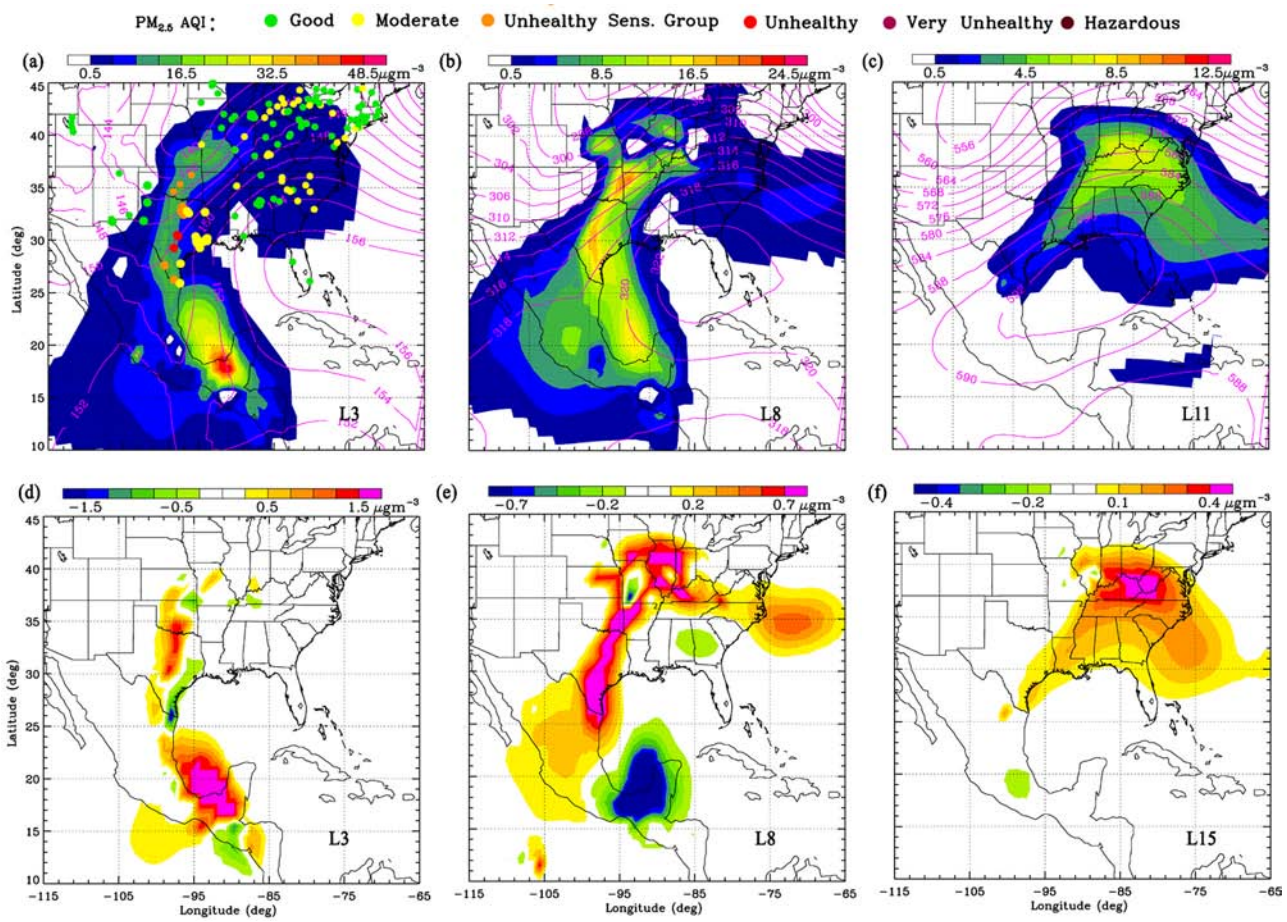

Figure 10. (a–c) Distribution of smoke mass concentration at model third, eighth and eleventh layers above the surface (indicated as L3, L8 and L11 at the bottom right of each plot, respectively) at 1500 UTC (1000 LT) on 10 May 2003. The results are from SMKRAD experiment. Also overlaid is the geopotential height (in unit of 10 m) at 850 mb, 700 mb, and 500 mb, the pressure levels that are close to L3, L8, and L11, respectively. Color-coded dots in Figure 10a indicate the air quality category in different EPA $PM_{2.5}$ measurement stations [*Wang et al.*, 2006]. (d–f) Differences of smoke mass concentration between SMKRAD and NSMKRAD simulations at aforementioned layers, respectively.

the upper layer). This explains why SMKRAD case has a relative larger AOT than NSMKRAD case (Figure 7e).

[38] The above investigation only focused on 30-day averages. An interesting question to pose is if the importance of smoke radiative impacts and feedbacks are necessary for consideration in air quality modeling that focuses on smaller timescales (hourly to daily). Previous theoretical studies [*Park et al.*, 2001] and observations [*Taubman et al.*, 2004] have indicated that aerosol direct radiative effects have an important implication for photochemical processes such as ozone formation. The photons reflected by the smoke layer can result in more ozone formation above the smoke layer, yet less ozone is produced beneath the smoke layer where the amount of photons is reduced by the smoke radiative extinction [*Dickerson et al.*, 1997]. It was also observed and numerically verified in the current study that smoke radiative effects increase the atmospheric stability, which in turn traps more smoke particles in the lower PBL near the surface [e.g., *Robock*, 1988; *Taubman et al.*, 2004]. On the basis of the above observations as well as previous 1D theoretical analysis and current 3D simulations, it is therefore clear that in principle, the (smoke) aerosol radiative impacts should be considered in air quality modeling, although whether the model uncertainty itself would outweigh aerosol radiative impacts is another issue. Recently, using data collected during the Nashville southern oxidants studies, *Zamora et al.* [2003] demonstrated the need for incorporating aerosol radiative impacts in the MM5 models to produce the realistic radiative irradiance, temperature fields and PBL parameters that drive the air quality models. The aerosol radiation and transport components are also now being integrated into the WRF chemistry models (WRF-CHEM) [*Grell et al.*, 2004]. In this study, with our 3D simulations, we further found that the coupling between the smoke radiative impacts and atmospheric dynamics has significant implications for the air quality modeling.

[39] Figure 10 shows the smoke mass distribution in different model layers (Figures 10a–10c) and smoke mass difference between SMKRAD and NSMKRAD in these layers (Figure 10d–10f) on 10 May 2003. Also shown is the color-coded $PM_{2.5}$ air quality category in various $PM_{2.5}$ observation stations in the SEUS on this day. The region with high smoke concentration matches well with areas that are in the unhealthy air quality categories. Of particular

interest is a narrow south-north belt from southeastern Texas to central Oklahoma, where all $PM_{2.5}$ stations indicated an unhealthy air quality category (Figure 10a). Interestingly, this is also the zone which shows the large smoke mass difference between SMKRAD and NSMKRAD. Positive smoke mass difference is found in the lower boundary layer (Figure 10d), which is expected (because of the aforementioned smoke radiative feedbacks). However, what is unexpected is that not all upper PBLs exhibit the negative difference of smoke mass concentration (Figures 10e and 10f). Indeed, the negative difference only exists in the smoke source region and over the Gulf of Mexico (Figures 10e and 10f). So what is the reason for the positive difference of smoke mass concentration in the SEUS in upper layers (Figures 10e and 10f)? Our 3D animations (not shown) indicated that the air mass in the upper layers over the SEUS originates from the lower boundary layer in the smoke source region. Because of smoke radiative feedbacks, the smoke concentration is higher in SMKRAD case. Under the southerly flow of a high pressure system centered over the Gulf of Mexico (Figures 10a–10c), this smoke layer with higher concentration of smoke particles was maintained in the nocturnal boundary layer during its transport to the southern Texas. When it moved northward and started to be in the front of a trough in southern Texas, it was uplifted under the influence of the low-level convergence and upward motion caused by this trough (Figures 10a–10c). Thus positive difference of smoke mass concentration is still maintained in the SMKRAD and NSMKRAD cases, even after the long-range transport. The difference of smoke mass concentration is about 5% (or 1.5 μgm^{-3}) in lower level, and about 10% in the upper level (figure not shown). Therefore the smoke radiative impacts, when coupled with favorable dynamical conditions, might have important implications for air quality modeling and other related studies such as cloud-aerosol interaction.

4. Discussion and Conclusion

[40] Using a coupled aerosol-radiation-meteorology model, we have quantified the direct radiative impacts of Central American biomass burning smoke aerosols on the surface energy budget, air temperature, and atmospheric boundary layer processes. Unlike previous 1D theoretical analysis [e.g., *Atwater*, 1971a, 1971b; *Bergstrom*, 1973; *Ackerman*, 1977; *Carlson and Benjamin*, 1980; *Yu et al.*, 2002] or the investigations using regional climate models [*Chung and Zhang*, 2004; *Davison et al.*, 2004], this study benefits from the assimilation of GOES-derived hourly smoke emission, and therefore realistically simulates the horizontal and vertical distribution of smoke and smoke radiative impacts. The diurnal change of smoke AOT (with peak value in later afternoon) in the source region is successfully simulated in the RAMS-AROMA. Consistency is also found between the model and in situ measurements on the temporal evolution of AOT in the downwind regions. Our limited validation showed the improvement in simulating the 2mT by incorporating the smoke radiative impacts in the model.

[41] Quantitatively, we found that smoke AOT in the source region is 0.18 (in 30-day 24-hour average), two times larger than that in the downwind region. However, the reduction of DSWI, SEH, LTH, and PBLH in the source and downwind regions are not proportional to their AOT amount, because of the difference in solar zenith angles, relative humidity, and surface characteristics (e.g., albedo, soil moisture, etc). In particular, the changes of 2mT and DTR in the source regions are 0.21°C and 0.31°C, respectively; only slightly larger than 0.15°C and 0.26°C in the downwind Texas region. More importantly, we showed that the smoke radiative impacts enhance the atmospheric stability by reducing (increasing) the temperature near the surface (in upper boundary layer), and result in favorable mechanisms to have more smoke aerosols trapped in the lower PBL. However, this is not the case for over the ocean surface that has a large heat capacity and deep mixing depth, which make it less sensitive thereby resulting in minimal response to the reduction of DSWI by smoke aerosols, at least on short-term scales. Over the ocean we found that smoke absorption results in an increase of temperature in both lower and upper boundary layers. These smoke radiative feedbacks, when coupled with dynamical processes, might have important implications for air quality modeling. Indeed, aerosol-radiation-meteorology coupling is identified by the U.S. weather research program as one of priorities for the improving the air quality modeling [*Dabberdt et al.*, 2004]. This study showed that assimilating the satellite-derived high temporal resolution emission products into meteorological models (such as in RAMS-AROMA) provides a feasible methodology toward that direction.

[42] Since smoke direct radiative impacts on the surface energy budget and atmospheric temperature profile are not negligible, they might also produce feedback on the evaporation process, cloud formation as well as precipitation distribution [*Menon et al.*, 2002]. However, current simulation of precipitation and cloud formation in GCMs and most meteorological models still highly depends on the cloud parameterization scheme that needs further improvement. Recently, the explicit modeling of cloud microphysical processes has showed advances in pursing the linkage of aerosol to the cloud formation processes [*Ackerman et al.*, 2000; *Feingold et al.*, 2001]. We are planning to conduct further studies about the smoke impacts on the cloud and precipitation by developing the size-resolved smoke transportation schemes as well as using explicit cloud microphysics schemes [*Meyers et al.*, 1997] in RAMS-AROMA.

[43] **Acknowledgments.** This research was supported by NASA's Radiation Sciences, Interdisciplinary sciences (FLAMBE) and ACMAP programs. J. Wang was supported by the NASA Earth System Science Graduate Fellowship. While in Harvard, J. Wang was supported by the NOAA Postdoctoral Fellowship Program in Climate and Global Change under the administration of UCAR visiting scientist program. We are grateful to Udaysankar Nair for his constructive comments while writing this manuscript and Jerry Harrington for providing the data of cloud radiative properties in RAMS. We thank Jeffrey Reid and Elaine Prins for the fire and smoke emission data and NASA Goddard DAAC for the MODIS data. The NIFMR AOT and solar irradiance data were obtained from the DOE ARM program, and we are thankful to Joseph Michalsky and Chuck Long for their guidance in using the data. We also thank two anonymous reviewers for their suggestions that resulted in Figure 9.

References

Ackerman, A. S., O. B. Toon, D. E. Stevens, A. J. Heymsfield, V. Ramanathan, and E. J. Welton (2000), Reduction of tropical cloudiness by soot, *Science*, *288*, 1042–1047.

Ackerman, S. A., and S. K. Cox (1982), The Saudi Arabian heat low: Aerosol distributions and thermodynamics structure, *J. Geophys. Res.*, *87*, 8991–9002.

Ackerman, T. (1977), A model of the effect of aerosols on urban climates with particular application to the Los Angeles Basin, *J. Atmos. Sci.*, *34*, 531–547.

Alpert, P., Y. J. Kaufman, Y. Shay-El, D. Tanre, A. D. Silva, S. Schubert, and J. H. Joseph (1998), Quantification of dust-forced heating of the lower troposphere, *Nature*, *395*, 367–370.

Andrews, E., P. J. Sheridan, J. A. Ogren, and R. Ferrare (2004), In situ aerosol profiles over the Southern Great Plains cloud and radiation test bed site: 1. Aerosol optical properties, *J. Geophys. Res.*, *109*, D06208, doi:10.1029/2003JD004025.

Atwater, M. A. (1971a), Radiative effects of pollutants in the atmospheric boundary layer, *J. Atmos. Sci.*, *28*, 1367–1373.

Atwater, M. A. (1971b), The radiation budget for polluted layers of the urban environment, *J. Appl. Meteorol.*, *10*, 205–214.

Bergstrom, R. (1973), Modeling of the effects of gaseous and particulate pollutants in the urban atmosphere. Part I: Thermal structure, *J. Appl. Meteorol.*, *12*, 901–902.

Carlson, T. N., and S. G. Benjamin (1980), Radiative heating rate of Saharan dust, *J. Atmos. Sci.*, *37*, 193–213.

Carmichael, G. R., et al. (2003), Regional-scale chemical transport modeling in support of the analysis of observations obtained during the TRACE-P experiment, *J. Geophys. Res.*, *108*(D21), 8823, doi:10.1029/2002JD003117.

Cautenet, G., M. Legrand, S. Cautenet, B. Bonnel, and G. Brogniez (1992), Thermal impact of Saharan dust over land. Part I: Simulation, *J. Appl. Meteorol.*, *31*, 166–180.

Chang, H., and T. T. Charalampopoulos (1990), Determination of the wavelength dependences of refractive indices of flame soot, *Proc. R. Soc. London, Ser A.*, *430*, 577–591.

Chen, S.-J., Y.-H. Kuo, W. Ming, and H. Ying (1995), The effect of dust radiative heating on low-level frontogenesis, *J. Atmos. Sci.*, *52*, 1414–1420.

Chin, M., P. Ginoux, S. Kinne, O. Torres, B. N. Holben, B. N. Duncan, R. V. Martin, J. A. Logan, A. Higurashi, and T. Nakajima (2002), Tropospheric aerosol optical thickness from the GOCART model and comparisons with satellite and Sun photometer measurements, *J. Atmos. Sci.*, *59*, 461–483.

Chin, M., A. Chu, R. Levy, L. Remer, Y. Kaufman, B. Holben, T. Eck, P. Ginoux, and Q. Gao (2004), Aerosol distribution in the Northern Hemisphere during ACE-Asia: Results from global model, satellite observations, and Sun photometer measurements, *J. Geophys. Res.*, *109*, D23S90, doi:10.1029/2004JD004829.

Christopher, S. A., and J. Zhang (2002), Daytime variation of shortwave direct radiative forcing of biomass burning aerosols from GOES 8 imager, *J. Atmos. Sci.*, *59*, 681–691.

Christopher, S. A., X. Li, R. M. Welch, P. V. Hobbs, J. S. Reid, and T. F. Eck (2000), Estimation of downward and top-of-atmosphere shortwave irradiances in biomass burning regions during SCAR-B, *J. Appl. Meteorol.*, *39*, 1742–1753.

Christopher, S. A., J. Wang, Q. Ji, and S. Tsay (2003), Estimation of diurnal shortwave dust aerosol radiative forcing during PRIDE, *J. Geophys. Res.*, *108*(D19), 8596, doi:10.1029/2002JD002787.

Chung, C. E., and G. J. Zhang (2004), Impact of absorbing aerosol on precipitation: Dynamic aspects in association with convective available potential energy and convective parameterization closure and dependence on aerosol heating profile, *J. Geophys. Res.*, *109*, D22103, doi:10.1029/2004JD004726.

Colarco, P. R., M. R. Schoeberl, B. G. Doddridge, L. T. Marufu, O. Torres, and E. J. Welton (2004), Transport of smoke from Canadian forest fires to the surface near Washington, D.C.: Injection height, entrainment, and optical properties, *J. Geophys. Res.*, *109*, D06203, doi:10.1029/2003JD004248.

Cotton, W. R., et al. (2003), RAMS 2001: Current status and future directions, *Meteorol. Atmos. Phys.*, *82*, 5–29.

Crutzen, P. J., and M. O. Andreae (1990), Biomass burning in the tropics: Impact on atmospheric chemistry and biogeochemical cycles, *Science*, *250*, 1669–1678.

Crutzen, P. J., L. E. Heidt, J. P. Krasnec, W. H. Pollock, and W. Seiler (1979), Biomass burning as a source of atmospheric gases CO, H_2, N_2O, NO, CH_3Cl and COS, *Nature*, *282*, 253–256.

Dabberdt, W. F., et al. (2004), Meteorological research needs for improved air quality forecasting, report of the 11th prospectus development team of the U.S. weather research program, *Bull. Am. Meteorol. Soc.*, *85*, 563–586, doi:10.1175/BAMS-85-4-563.

Davison, P. S., D. L. Roberts, R. T. Arnold, and R. N. Colvile (2004), Estimating the direct radiative forcing due to haze from the 1997 forest fires in Indonesia, *J. Geophys. Res.*, *109*, D10207, doi:10.1029/2003JD004264.

Dickerson, R. R., S. Kondragunta, G. Stenchikov, K. L. Civerolo, B. G. Doddridge, and B. N. Holben (1997), The impact of aerosols on solar ultraviolet radiation and photochemical smog, *Science*, *278*, 827–830.

Eck, T. F., et al. (2003), Variability of biomass burning aerosol optical characteristics in southern Africa during the SAFARI 2000 dry season campaign and a comparison of single scattering albedo estimates from radiometric measurements, *J. Geophys. Res.*, *108*(D13), 8477, doi:10.1029/2002JD002321.

Feingold, G., L. A. Remer, J. Ramaprasad, and Y. J. Kaufman (2001), Analysis of smoke impact on clouds in Brazilian biomass burning regions: An extension of Twomey's approach, *J. Geophys. Res.*, *106*, 22,907–22,922.

Feingold, G., H. Jiang, and J. Y. Harrington (2005), On smoke suppression of clouds in Amazonia, *Geophys. Res. Lett.*, *32*, L02804, doi:10.1029/2004GL021369.

Fu, Q., and K. N. Liou (1993), Parameterization of the radiative properties of cirrus clouds, *J. Atmos. Sci.*, *50*, 2008–2025.

Grell, G., J. Dudhia, and D. Stauffer (1995), A description of the Fifth-Generation Penn State/NCAR Mesoscale Model (MM5), *NCAR/TN-398+STR*, 122 pp., Natl. Cent. for Atmos. Res., Boulder, Colo.

Grell, G. A., S. E. Penkham, R. Schmitz, and S. A. Mckeen (2004), Fully coupled "online" chemistry with the WRF model, paper presented at Sixth Conference on Atmospheric Chemistry, Air Quality in Megacitites, Am. Meteorol. Soc., Seattle, Wash.

Harrington, J. Y., and P. Q. Olsson (2001), A method for the parameterization of cloud optical properties in bulk and bin microphysical models. Implications for arctic cloudy boundary layers, *Atmos. Res.*, *57*, 51–80.

Ichoku, C., L. A. Remer, and T. F. Eck (2005), Quantitative evaluation and intercomparison of morning and afternoon Moderate Resolution Imaging Spectroradiometer (MODIS) aerosol measurements from Terra and Aqua, *J. Geophys. Res.*, *110*, D10S03, doi:10.1029/2004JD004987.

Intergovernmental Panel on Climate Change (2001), *Climate Change 2001: The Scientific Basis—Contribution of Working Group I to the Third Assessment Report of the Intergovernmental Panel on Climate Change*, edited by J. T. Houghton et al., 881 pp., Cambridge Univ. Press, New York.

Jacobson, M. Z. (2001), Strong radiative heating due to the mixing state of black carbon in atmospheric aerosols, *Nature*, *409*, 695–697.

Kalnay, E., et al. (1996), The NCEP/NCAR 40-year reanalysis project, *Bull. Am. Meteorol. Soc.*, *77*, 437–471.

Kaufman, Y. J., et al. (1998), The Smoke, Clouds and Radiation Experiment in Brazil (SCAR-B), *J. Geophys. Res.*, *103*, 31,783–31,808.

Koren, I., Y. J. Kaufman, L. A. Remer, and J. V. Martins (2004), Measurement of the effect of Amazon smoke on inhabitation of cloud formation, *Science*, *303*, 1342–1345.

Kotchenruther, R. A., and P. V. Hobbs (1998), Humidification factors of aerosols from biomass burning in Brazil, *J. Geophys. Res.*, *103*, 32,081–32,089.

Liousse, C., J. E. Penner, C. C. Chuang, J. J. Walton, and H. Eddleman (1996), A global three-dimensional model study of carbonaceous aerosols, *J. Geophys. Res.*, *101*, 19,441–19,432.

Long, C. N., and T. A. Ackerman (2000), Identification of clear skies from broadband pyranometer measurements and calculation of downwelling shortwave cloud effects, *J. Geophys. Res.*, *105*, 15,609–15,626.

Long, C. N., and K. L. Gaustad (2004), The shortwave clear-sky detection and fitting algorithm: Algorithm operational details and explanations, *Tech. Rep. ARM TR-004*, Atmospheric Radiation Measurement Program, U.S. Dep. of Energy, Washington, D. C. (Available at http://www.arm.gov/publications/tech_reports/arm-tr-004.pdf)

Mellor, G. L., and T. Yamada (1974), A hierarchy of turbulent closure models for planetary boundary layers, *J. Atmos. Sci.*, *31*, 1791–1806.

Menon, S., J. Hansen, L. Nazarenko, and Y. Luo (2002), Climate effect of black carbon aerosols in China and India, *Science*, *297*, 2250–2252.

Meyers, M. P., R. L. Walko, J. Y. Harrington, and W. R. Cotton (1997), New RAMS cloud microphysics parameterization. Part II: The two moment scheme, *Atmos. Res.*, *45*, 3–39.

Michalsky, J. J., J. A. Schlemmer, W. E. Berkheiser, J. L. Berndt, L. C. Harrison, N. S. Laulainen, N. R. Larson, and J. C. Barnard (2001), Multiyear measurements of aerosol optical thickness in the Atmospheric Radiation Measurement and quantitative links programs, *J. Geophys. Res.*, *106*, 12,099–12,107.

Park, R. J., G. L. Stenchikov, K. E. Pickering, R. R. Dickerson, D. J. Allen, and S. Kondragunta (2001), Regional air pollution and its radiative forcing: Studies with a single-column chemical and radiation transport model, *J. Geophys. Res.*, *106*, 28,751–28,770.

Park, R. J., D. J. Jacob, M. Chin, and R. V. Martin (2003), Sources of carbonaceous aerosols over the United States and implications for natural visibility, *J. Geophys. Res.*, *108*(D12), 4355, doi:10.1029/2002JD003190.

Pielke, R. A., R. L. Walko, J. L. Eastman, W. A. Lyons, R. A. Stocker, M. Uliasz, and C. J. Tremback (1992), A comprehensive meteorological modeling system—RAMS, *Meteorol. Atmos. Phys.*, *49*, 69–91.

Penner, J. E., R. Dickinson, and C. O'Neill (1992), Effects of aerosol from biomass burning on the global radiation budget, *Science*, *256*, 1423–1434.

Peppler, R. A., et al. (2000), ARM southern great plains site observations of the smoke pall associated with the 1998 Central American fires, *Bull. Am. Meteorol. Soc.*, *81*, 2563–2592.

Prins, E. M., J. M. Feltz, W. P. Menzel, and D. E. Ward (1998), An overview of GOES-8 diurnal fire and smoke results for SCAR-B and the 1995 fire season in South America, *J. Geophys. Res.*, *103*, 31,821–31,835.

Ramanathan, V. P., J. Crutzen, J. T. Kiehl, and D. Rosenfeld (2001), Aerosols, climate, and the hydrological cycle, *Science*, *294*, 2119–2124.

Reid, J. S., E. M. Prins, D. L. Westphal, C. C. Schmidt, K. A. Richardson, S. A. Christopher, T. F. Eck, E. A. Reid, C. A. Curtis, and J. P. Hoffman (2004), Real-time monitoring of South American smoke particle emissions and transport using a coupled remote sensing/box-model approach, *Geophys. Res. Lett.*, *31*, L06107, doi:10.1029/2003GL018845.

Reid, J. S., T. F. Eck, S. A. Christopher, R. Koppmann, O. Dubovik, D. P. Eleuterio, B. N. Holben, E. A. Reid, and J. Zhang (2005), A review of biomass burning emissions part III: Intensive optical properties of biomass burning particles, *Atmos. Chem. Phys.*, *5*, 827–849.

Remer, L. A., et al. (2005), The MODIS aerosol algorithm, product, and validation, *J. Atmos. Sci.*, *62*, 947–973.

Robock, A. (1988), Enhancement of surface cooling due to forest fire smoke, *Science*, *242*, 911–913.

Rogers, C. M., and K. P. Bowman (2001), Transport of smoke from the Central American fires of 1998, *J. Geophys. Res.*, *106*, 28,357–28,368.

Russell, P. B., S. A. Kinne, and R. W. Bergstrom (1997), Aerosol climate effects: Local radiative forcing and column closure experiments, *J. Geophys. Res.*, *102*, 9397–9408.

Schafer, J. S., T. F. Eck, B. N. Holben, P. Artaxo, M. A. Yamasoe, and A. S. Procopio (2002), Observed reductions of total solar irradiance by biomass-burning aerosols in the Brazilian Amazon and Zambian Savanna, *Geophys. Res. Lett.*, *29*(17), 1823, doi:10.1029/2001GL014309.

Seibert, P., F. Beyrich, S.-E. Gryning, S. Joffre, A. Rasmussen, and P. Tercier (2000), Review and intercomparison of operational methods for the determination of the mixing height, *Atmos. Environ.*, *34*, 1001–1027.

Stephens, G. L. (1984), The parameterization of radiation for numerical weather prediction and climate models, *Mon. Weather Rev.*, *12*, 826–867.

Swap, R. J., H. J. Annegarn, J. T. Suttles, M. D. King, S. Platnick, J. L. Privette, and R. J. Scholes (2003), Africa burning: A thematic analysis of the Southern African Regional Science Initiative (SAFARI 2000), *J. Geophys. Res.*, *108*(D13), 8465, doi:10.1029/2003JD003747.

Taubman, B. F., L. T. Marufu, B. L. Vant-Hull, C. A. Piety, B. G. Doddridge, R. R. Dickerson, and Z. Li (2004), Smoke over haze: Aircraft observations of chemical and optical properties and the effects on heating rates and stability, *J. Geophys. Res.*, *109*, D02206, doi:10.1029/2003JD003898.

Tegen, I., P. Hollrig, M. Chin, I. Fung, D. Jacob, and J. Penner (1997), Contribution of different aerosols to the global aerosol extinction optical thickness: Estimates from model results, *J. Geophys. Res.*, *102*, 23,895–23,915.

Twomey, S. (1977), The influence of pollution on the shortwave albedo of clouds, *J. Atmos. Sci.*, *34*, 1149–1152.

Walko, R. L., W. R. Cotton, M. P. Meyers, and J. Y. Harrington (1995), New RAMS cloud microphysics parameterization, part I: The single-moment scheme, *Atmos. Res.*, *38*, 29–62.

Walko, R. L., et al. (2000), Coupled atmosphere-biophysics-hydrology models for environmental modeling, *J. Appl. Meteorol.*, *39*, 931–944.

Wang, J. (2005), Air quality and radiative impacts of long-range transported aerosols over the southeastern United States, Ph.D. dissertation, Dep. of Atmos. Sci., Univ. of Ala., Huntsville.

Wang, J., U. S. Nair, and S. A. Christopher (2004), GOES 8 aerosol optical thickness assimilation in a mesoscale model: Online integration of aerosol radiative effects, *J. Geophys. Res.*, *109*, D23203, doi:10.1029/2004JD004827.

Wang, J., S. A. Christopher, U. S. Nair, J. S. Reid, E. M. Prins, J. Szykman, and J. L. Hand (2006), Mesoscale modeling of Central American smoke transport to the United States: 1. "Top-down" assessment of emission strength and diurnal variation impacts, *J. Geophys. Res.*, *111*, D05S17, doi:10.1029/2005JD006416.

Westphal, D. L., and O. B. Toon (1991), Simulation of microphysical, radiative, and dynamical processes in a continental-scale forest smoke plume, *J. Geophys. Res.*, *96*, 22,379–22,400.

Yu, H., S. C. Liu, and R. E. Dickinson (2002), Radiative effects of aerosols on the evolution of the atmospheric boundary layer, *J. Geophys. Res.*, *107*(D12), 4142, doi:10.1029/2001JD000754.

Zamora, R. J., S. Solomon, E. G. Dutton, J. W. Bao, M. Trainer, R. W. Portmann, A. B. White, D. W. Nelson, and R. T. McNider (2003), Comparing MM5 radiative fluxes with observations gathered during the 1995 and 1999 Nashville southern oxidants studies, *J. Geophys. Res.*, *108*(D2), 4050, doi:10.1029/2002JD002122.

S. A. Christopher, Department of Atmospheric Science, University of Alabama, 320 Sparkman Drive, Huntsville, AL 35805, USA. (sundar@nsstc.uah.edu)

J. Wang, Division of Engineering and Applied Science, Pierce Hall, Room G3F, Harvard University, 29 Oxford Street, Cambridge, MA 02138, USA. (junwang@fas.harvard.edu)